A MESHLESS METHOD WITH ENRICHED BASIS FUNCTIONS FOR SINGULARITY PROBLEMS

by

Won-Tak Hong

A dissertation submitted to the faculty of
the University of North Carolina at Charlotte
in partial fulfillment of the requirements
for the degree of Doctor of Philosophy in
Applied Mathematics

Charlotte

2009

Approved by:

Dr. Hae-Soo Oh

Dr. Thomas R. Lucas

Dr. Boris Vainberg

Dr. Ronald E. Smelser

ABSTRACT

WON-TAK HONG. A Meshless method with enriched basis functions for singularity problems. (Under the direction of DR. HAE-SOO OH)

For the last several decades, the Finite Element Method (FEM) has been a powerful tool in solving challenging science and engineering problems, especially when solution domains have complex geometry. However the mesh refinements and construction of higher order interpolation fields were prominent difficulties in classical finite element analysis.

In order to alliveate the difficulties of classical finite element method, the meshless methods were introduced. Meshless methods appear in several different names such as Element Free Galerkin Method (EFGM), h-p cloud Method, Partition of Unity Finite Element Method (PUFEM), Generalized Finite Element Method (GFEM), and Extended Finite Element Method (XFEM). In this dissertation, we are concerned with enriched GFEM. Unlike classical finite element methods, these meshless methods use meshes minimally or not at all. This feature becomes powerful when it comes to model crack propagation, large deformation, etc because re-meshing is unnecessary.

A partition of unity is an essential component of GFEM. The partition of unity function employed in this dissertation, is unique in the following sense: First, the partition of unity functions are highly regular, whereas most GFEM in the literature use piecewise C^0-partition of unity functions. The highly regular partition of unity functions with appropriate smooth local approximation functions enables us to have highly regular global basis functions. Second, if polynomial local approximation functions that satisfy the Kronecker delta property are chosen, the global basis functions become smooth piecewise polynomials, and hence numerical integrations become exact and imposing essential boundary conditions become simple. Third, the partition of unity shape functions designed to have flat-top do not yield an ill-conditioned stiff-

ness matrix. Furthermore, a partition of unity for a non-convex domain is introduced to deal with an elasticity problem on a cracked elastic medium.

The most powerful aspect of GFEM is the freedom to choose any desired local approximation functions. By choosing highly smooth local basis functions, it would be possible to solve high order PDEs such as biharmonic and polyharmonic partial differential equations without using Hermite finite elements that are extremely difficult to implement. Moreover, when a given problem has strong singularities, using various types of singular functions, the approximation space can be enriched to capture the singularities without regenerating the whole mesh or refining the meshes in the adaptive way.

In this dissertation, GFEM with enriched basis functions is used to solve elliptic boundary value problems containing singularities. In Chapter 2, our meshless method is applied to solve the Motz problem that has jump boundary data singularity. In Chapter 3, we use our method to get highly accurate stress analysis of cracked elastic domains. We demonstrate that the proposed approach yields highly accurate numerical solution of the Motz problem as well as accurate stress analysis of cracked elastic domains. We also will show that the meshless method, GFEM with enriched basis functions, yields the improved results, compared with performance of other existing methods. Finally, we introduce a new approach to estimate the stress intensity factor.

DEDICATION

To my loving wife Sujin

ACKNOWLEDGEMENTS

I would like to express my sincere gratitude and appreciation to my advisor, Hae-Soo Oh, for his guidance, and for ensuring financial support throughout my studies. He was not only a great teacher but also a wonderful mentor, and model. Without his encouragement and guidance this dissertation would not have materialized.

I am also grateful to the members of my committee for taking the time to guide me through my dissertation. Especially I would like to express special thanks to Dr. Thomas R. Lucas who showed me the beauty of numerical linear algebra and for his insightful remarks, and valuable comments. I am also grateful to Dr. Boris Vainberg who taught me the distribution theory and partial differential equations. Dr. Ronald E. Smelser has generously given his time and expertise to better my work.

I wish to express my profound thanks to my parents and wife for their selfless sacrifices that they made in allowing me to pursue my education.

Special thanks goes to Michael and Tammy Toney, for providing a constant source of encouragement and support, and for their prayer. I thank my brothers and sisters in Christ at University Hills Baptist Church for an amazing friendship within the Lord. I feel very humbled to study his creation in the view of applied mathematics. I truly believe that, not only do we find the Divine in the process of our work, I see God's glory in the creation that we study. I agree what was written in the scripture: For since the creation of the world God's invisible qualities-his eternal power and divine nature-have been clearly seen, being understood from what has been made, so that men are without excuse, Romans 1:20. To see God's creation, the beauty beyond partial differential equations, added another dimension of pleasure to the entire journey. I am grateful for God's provision and grace.

TABLE OF CONTENTS

LIST OF FIGURES

LIST OF TABLES

LIST OF ABBREVIATIONS

FEM	Finite Element Methods
h-FEM	h-version Finite Element Methods
p-FEM	p-version Finite Element Methods
GFEM	Generalized Finite Element Methods
PU	Partition of Unity
PUFEM	Partition of Unity Finite Element Methods
EFGM	Element Free Galerkin Methods
RKEM	Reproducing Kernel Element Methods
RPP	Reproducing Polynomial Particle
RKPM	Reproducing Kernel Particle Methods
RPPM	Reproducing Polynomial Particle Methods
RSPM	Reproducing Singularity Particle Methods
MAM	Method of Auxiliary Mapping
SIF	Stress Intensity Factor

CHAPTER 1: ENRICHED GENERALIZED FINITE ELEMENT METHODS

1.1 Introduction

Since it was introduced in the 1950s, the Finite Element Method (FEM) has become the most popular and powerful tool in solving challenging science and engineering problems, especially when solution domains have complex geometry (Ciarlet, 1991, Szabo and Babuska, 1991). However, the construction of higher order interpolation fields and mesh refinement has been a prominent difficulty in the finite element method.

In order to alleviate the constraints of the conventional method, generalized finite element methods (GFEM) have been introduced. These new approaches use meshes minimally or not at all. To name few of them : GFEM (Babuska et al., 2003, 2008), Element Free Galerkin Method (EFGM) (Lancaster and Salkauskas, 1981, Levin, 1998), h-p Cloud Method (Duarte and Oden, 1996), Partition of Unity Finite Element Method (PUFEM) (Babuska et al., 2003, Melenk et al., 1996, Strouboulis et al., 2003). Another non conventional FEM, closely related to GFEM, are Meshfree Particle Methods, such as Reproducing Kernel Particle Method (RKPM) (Han and Meng, 2001, Li and Liu, 2004) and Reproducing Kernel Element Method (RKEM) (Li and Liu, 2004, Li et al., 2004, Liu et al., 2004).

A partition of unity (PU) is an essential ingredient in the construction of approximation functions in GFEM. In this dissertation , highly smooth piecewise polynomial PU functions are used to make GFEM more effective in handling singularity problems.

1.2 Preliminaries

Let Ω be a domain in $\mathbb{R}^n$. Throughout this dissertation $\alpha, \beta, \cdots \in \mathbb{Z}^n$ indicate multi-indices and $x, y, \cdots \in \mathbb{R}^n$ denote points in $\mathbb{R}^n$ if there is no confusion. We adapt the conventional notation for a point x in $\mathbb{R}^n$ as $x = (x_1, x_2, \cdots, x_n)$ and for the multi-index α in $\mathbb{Z}^n$ as $\alpha = (\alpha_1, \alpha_2, \cdots, \alpha_n)$. For any non negative integer m, let $\mathcal{C}^m(\Omega)$ denote the space of all functions f such that f together with all its derivatives

$$D^\alpha f = D_x^\alpha f = \frac{\partial^{|\alpha|} f}{\partial^{\alpha_1} x_1 \partial^{\alpha_2} x_2 \cdots \partial^{\alpha_n} x_n}$$

of all orders $|\alpha| \leq n$, are continuous on Ω. In the following, a function $f \in \mathcal{C}^m(\Omega)$ is said to be a $\mathcal{C}^m$- function.

In the following definition, $H^k = H^k(\Omega)$ represents the **Sobolev space**.

Definition *For $f \in H^k(\Omega)$, the norm and the semi-norm, are defined by*

$$\|f\|_{k,\Omega} = \Big\{ \sum_{|\alpha| \leq k} \int_\Omega |D^\alpha f|^2 dx \Big\}^{1/2}, \quad \text{and } |f|_{k,\Omega} = \Big\{ \sum_{|\alpha| = k} \int_\Omega |D^\alpha f|^2 dx \Big\}^{1/2}.$$

respectively. The maximum norm of f is defined by

$$\|f\|_{\infty,\Omega} = ess\ sup \Big\{ |f(x)| : x \in \Omega \Big\}.$$

Definition *For given index set Λ, a family $\{O_k : k \in \Lambda\}$ of open subsets of $\mathbb{R}^n$ is said to be* **a point finite open covering** *of $\Omega \subseteq \mathbb{R}^n$ if there is a number M such that any $x \in \Omega$ lies in at most M open sets O_k and $\Omega \subseteq \bigcup_k O_k$.*

Definition *The* **support of** *f is defined by*

$$supp\ f = \overline{\{x \in \Omega : f(x) \neq 0\}}.$$

Definition *$\{\phi_k : k \in \Lambda\}$ is called a* **partition of unity (PU)** *subordinate to the covering $\{O_k : k \in \Lambda\}$ if there is a family $\{\phi_k : k \in \Lambda\}$ of Lipschitz functions in Ω that satisfy the following three conditions:*

(1) $\exists\ C$ *such that* $\|\phi_k\|_{\infty,\mathbb{R}^d} \leq C$ *for all* k.

(2) *supp* $(\phi_k) \subseteq \overline{O_k}$, *for each* $k \in \Lambda$.

(3) $\sum_{k\in\Lambda} \phi_k(x) = 1,\ \forall x \in \Omega$.

Here $\{O_k : k \in \Lambda\}$ *is a point finite open covering of a domain* Ω, *and* Λ *is an index set. The members of the covering* $\{O_k\}$ *are called* **patches**.

Definition *The uniform* B**-spline** b_n *of degree* n *is defined by the recursion*

$$b_n(x) = \int_{x-1}^{x} b_{n-1}(t)dt,$$

starting from the characteristic function $b_0(x)$ *of the unit interval* $[0, 1)$.

The B-splines have the following properties (Höllig, 2003):

- $b_n \in \mathcal{C}^{n-1}(\mathbb{R})$ is positive on $(0, n+1)$ and vanishes outside this interval.
- b_n is a piecewise polynomial: it is a polynomial of degree n on each interval $[k, k+1], k = 0, \cdots, n$.
- The B-spline of degree n is symmetric about $y = (n+1)/2$.
- (Recurrence Relation)

$$b_n(x) \quad = \quad \frac{x}{n} b_{n-1}(x) + \frac{n+1-x}{n} b_{n-1}(x-1).$$

- (Convolution Property)

$$b_{n+m+1}(x) = \int_{\mathbb{R}} b_m(x-y) b_n(y) dy.$$

- (Marsden's Identity) For $x, t \in \mathbb{R}$,

$$(x-t)^n \quad = \quad \sum_{k\in\mathbb{Z}} (k+1-t)\cdots(k+n-t) b_n(x-k).$$

From the Marsden identity, we have

$$\sum_k b_n(x-k) = 1,$$

which shows that b_n is a PU shape function. Moreover, the same identity can be applied to show the next property:

- Any monomial $x^l, 0 \leq l \leq n$ can be represented by $b_n(x-k), k \in \mathbb{Z}$, and hence, they are linearly independent.

Definition *A* **weight function (or window function)** $w(x)$, *is a non-negative continuous function with compact support that is defined as follows:*

$$w(x) = \begin{cases} (1-x^2)^l, & |x| \leq 1, \\ 0, & |x| > 1, \end{cases} \tag{1}$$

where l is a positive integer.

Remark $w(x)$ *is a $\mathcal{C}^{l-1}$-function.*

Definition *Let Λ be a finite index set and Ω be a bounded domain in $\mathbb{R}^n$. Let $\{x_j : j \in \Lambda\}$ be a set of a finite number of uniform or non-uniformly spaced particles in $\mathbb{R}^n$. Assume that k is a non-negative integer. Then the function $\phi_j(x)$ corresponding to the particles $x_j, j \in \Lambda$ is called the reproducing polynomial particle (RPP) shape function with the polynomial reproducing property of order k (or simply, "of reproducing order k") if it satisfies the following condition:*

$$\sum_{j\in\Lambda} (x_j)^\alpha \phi_j(x) = x^\alpha, \text{ for } x \in \Omega \subset \mathbb{R}^n \text{ and for } 0 \leq |\alpha| \leq k.$$

It is important to note that the RPP shape functions with the property of polynomial reproducing order k exactly interpolate all polynomials of degree $\leq k$.

An one dimensional example of a piecewise polynomial RPP shape function introduced by (Oh et al., 2007a,b) is as follows:

A $\mathcal{C}^2$-RPP shape function of reproducing order 2, $\phi_{([-2,2];2;2)}(x)$ is defined by (2). The graph of $\phi_{([-2,2];2;2)}(x)$ and $\frac{d}{dx}\phi_{([-2,2];2;2)}(x)$ are depicted below :

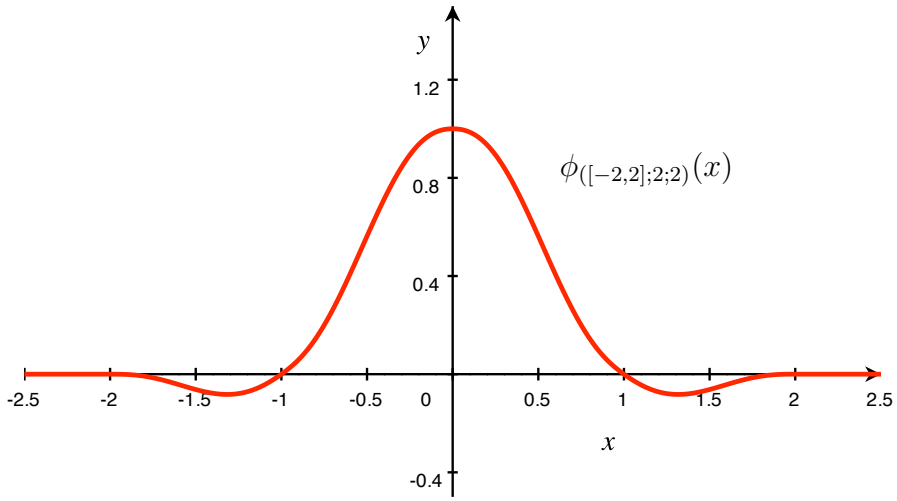

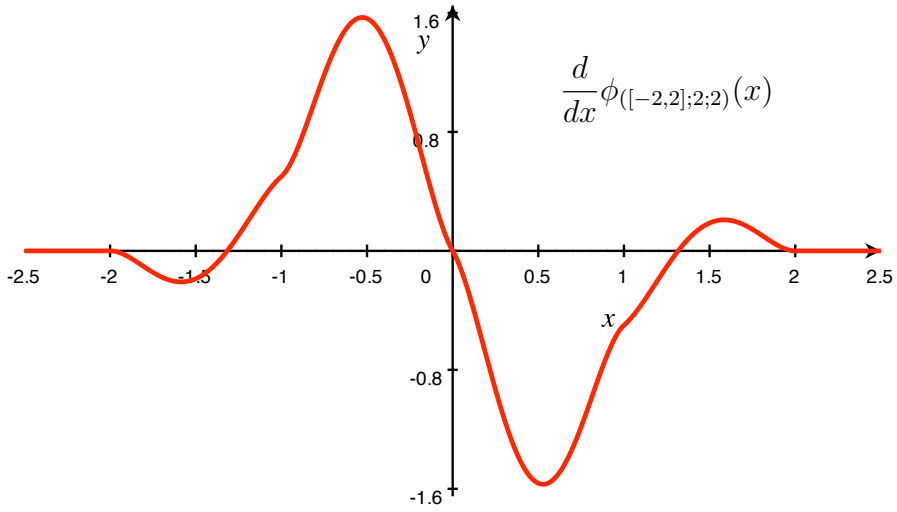

$$\phi_{([-2,2];2;2)}(x) = \begin{cases} -\frac{1}{2}(x+2)^3(x+1)(2x+1) & : \ x \in [-2,-1], \\ \frac{1}{2}(x+1)(6x^4+9x^3-2x+2) & : \ x \in [-1,0], \\ -\frac{1}{2}(x-1)(6x^4-9x^3+2x+2) & : \ x \in [0,1], \\ \frac{1}{2}(x-2)^3(x-1)(2x-1) & : \ x \in [1,2], \\ 0 & : \ x \notin [-2,2] \end{cases} \tag{2}$$

Both C^r-RPP funtions (Oh et al., 2007a,b) and B-**spline** (Höllig, 2003) are piece-wise polynomials. The C^r-RPP funtions satisfy almost all of the properties of B-splines, except the positivity and the convolution property. It is noteworthy that the piece-wise polynomial C^r-reproducing polynomial particle shape function introduced in (Oh et al., 2007a,b) satisfies the Kronecker delta property. However the B-**spline** functions have no Kronecker delta property.

The Galerkin Methods that uses C^r-RPP shape functions associated with particles are called the *Meshfree Method*. *Web*-spline (Weighted extended *b*-spline: extension of B-**spline**) is another popular meshless method. Other methods such as Element Free Galerkin Method (EFGM) and Reproducing Kernel Particle Method (RKPM) are also meshfree method(Atluri and Shen, 2002, Li and Liu, 2004). These methods do not use any mesh at all.

In contrast to meshfree methods, the *Generalized Finite Element Method* (GFEM) introduced in the next section, uses a *background mesh*. Thus, it is not completely meshfree. However, it is widely known as a meshless method because the usage of a background mesh is completely different from the mesh usage in the conventional finite element method. The former is for constructing partition of unity and the latter is for constructing basis. Unlike B-**spline** and C^r-RPP shape functions, the piecewise polynomial partition of unity shape functions do not have polynomial reproducing properties. However, in conjunction with appropriate local interpolation functions one can create highly regular basis functions. This enables us to solve higher order differential equations such as bi-harmonic or poly-harmonic problems (Oh et al., 2008) without the use of Hermite finite elements that are extremely difficult to implement. If local approximation functions are polynomials and have the Kronecker delta property, then the numerical integration becomes exact and imposing essential boundary conditions becomes simple. Moreover, having wide flat top partition of unity shape functions leads to a smaller matrix condition number. Finally, the ro-

bustness and simple assembling procedure of this method enables 3D implementation in a much simpler manner than the conventional finite element methods which makes this method more attractive(Oh et al., 2009). The next section is devoted to this piecewise polynomial partition of unity shape functions.

1.3 Methods of constructing partition of unity

A partition of unity is an essential ingredient in the Generalized Finite Element Method(GFEM). Let us consider various methods to construct a partition of unity.

[A] Linear Finite Element Mesh

A popular choice of partition of unity is the **linear** Finite Element Mesh. Let $\{\Psi_I, I = 1, 2, \cdots, M\}$ be a **linear** finite element basis, then $\sum_{I=1}^{M} \Psi_I = 1$ on Ω. Hence $\{\Psi_I, I = 1, 2, \cdots, M\}$ is a partition of unity subordinate to the finite element mesh. It is easy to use; however, the basis functions are only C^0 and result singular or almost singular stiffness matrix.

[B] The Shepard PU function

Shepard PU function is also widely known, however numerical integration becomes very expensive due to its fractional form (Babuska et al., 2004, Li and Liu, 2004).

Definition *The Shepard PU shape function $\phi^{(ss)}(x)$ is defined by*

$$\phi^{(ss)}(x) = \frac{w(x)}{w(x-1) + w(x) + w(x+1)}, \text{ for all } x \in \mathbb{R}$$

where $w(x)$ is a weight function. Then

$$\{\phi_j(x) = \phi^{ss}(x - j) : j \in \mathbb{Z}\}$$

is partition of unity.

Note that the regularity of $\phi^{(ss)}(x)$ depends on the regularity of $w(x)$. Although it is easy to construct a PU shape function in this way, we avoid using it because of the following limitations. First of all, due to the fact $\phi^{(ss)}(x)$ is a rational function, numerical integration becomes expensive; so it leads to lengthy computing time. Second, a large condition number is a well known fact for this PU function which requires nontrivial treatment such as special solver design. In order to overcome these limitations, polynomial based partition of unity methods were introduced.

[C] Smooth piecewise polynomial partition of unity

An optimal choice of a PU function in GFEM depends on the function being approximated. In appropriate circumstances, we have the followings:

1. A $\mathcal{C}^0$-PU function is the hat function.

2. A $\mathcal{C}^1$-PU function is the bubble function defined by

$$f(x) \;=\; \begin{cases} (\cos(\frac{\pi x}{2}))^2 & \text{if } |x|<1 \\ 0 & \text{if } |x|\geq 1, \end{cases}$$

   or the piecewise polynomial $\phi^{(pp)}_{g_2}$ defined below.

3. Piecewise polynomial $\mathcal{C}^n$-PU functions $\phi^{(pp)}_{g_{n+1}}$ for each positive integer n are constructed as follows :

Definition *For integers $n \geq 1$, we define a piecewise polynomial function by*

$$\phi^{(pp)}_{g_n}(x) = \begin{cases} \phi^L_{g_n}(x) := (1+x)^n g_n(x) & : \quad x \in [-1,0] \\ \phi^R_{g_n}(x) := (1-x)^n g_n(x) & : \quad x \in [0,1] \\ 0 & : \quad |x| \geq 1, \end{cases} \tag{3}$$

where $g_n(x) = a^{(n)}_0 + a^{(n)}_1(-x) + a^{(n)}_2(-x)^2 + \cdots + a^{(n)}_{n-1}(-x)^{n-1}$ whose coefficients are inductively constructed by the following recursion formula:

$$a^{(n)}_k = \begin{cases} 1, & \textit{if} \quad k=0 \\ \displaystyle\sum_{j=0}^{k} a^{(n-1)}_j, & \textit{if} \quad 0<k\leq n-2, \\ 2(a^{(n)}_{n-2}), & \textit{if} \quad k=n-1. \end{cases} \tag{4}$$

The coefficients $a^{(n)}_k$ can also be obtained by the following recursion formula:

$$a^{(n)}_k = \begin{cases} 1 & \text{if} \quad k=0, \\ (\dfrac{n+k-1}{k})a^{(n)}_{k-1} & \text{if} \quad 1\leq k\leq n-1. \end{cases} \tag{5}$$

Let us note the following:

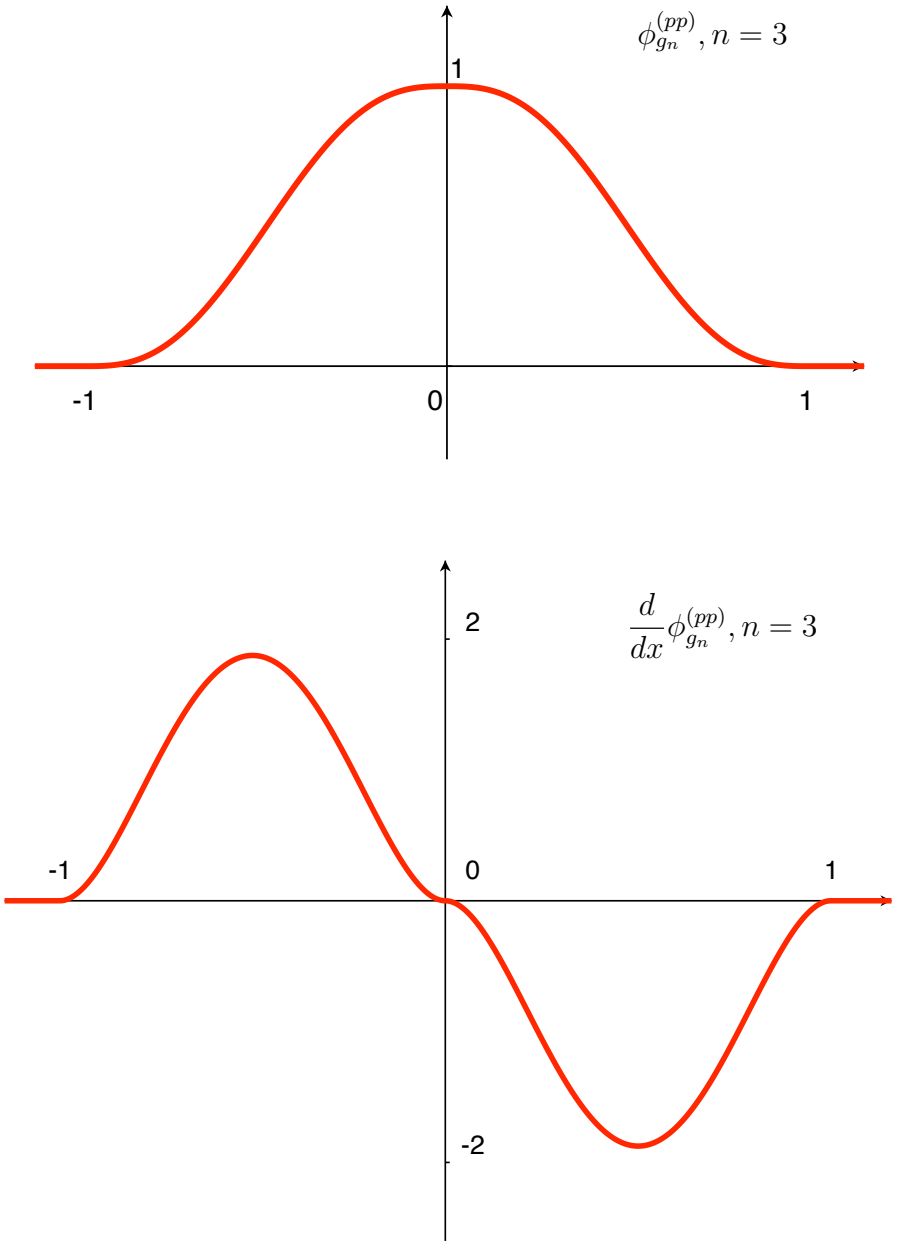

FIGURE 1: Two piece polynomial C^n partition of unity function, $\phi_{g_n}^{(pp)}$.

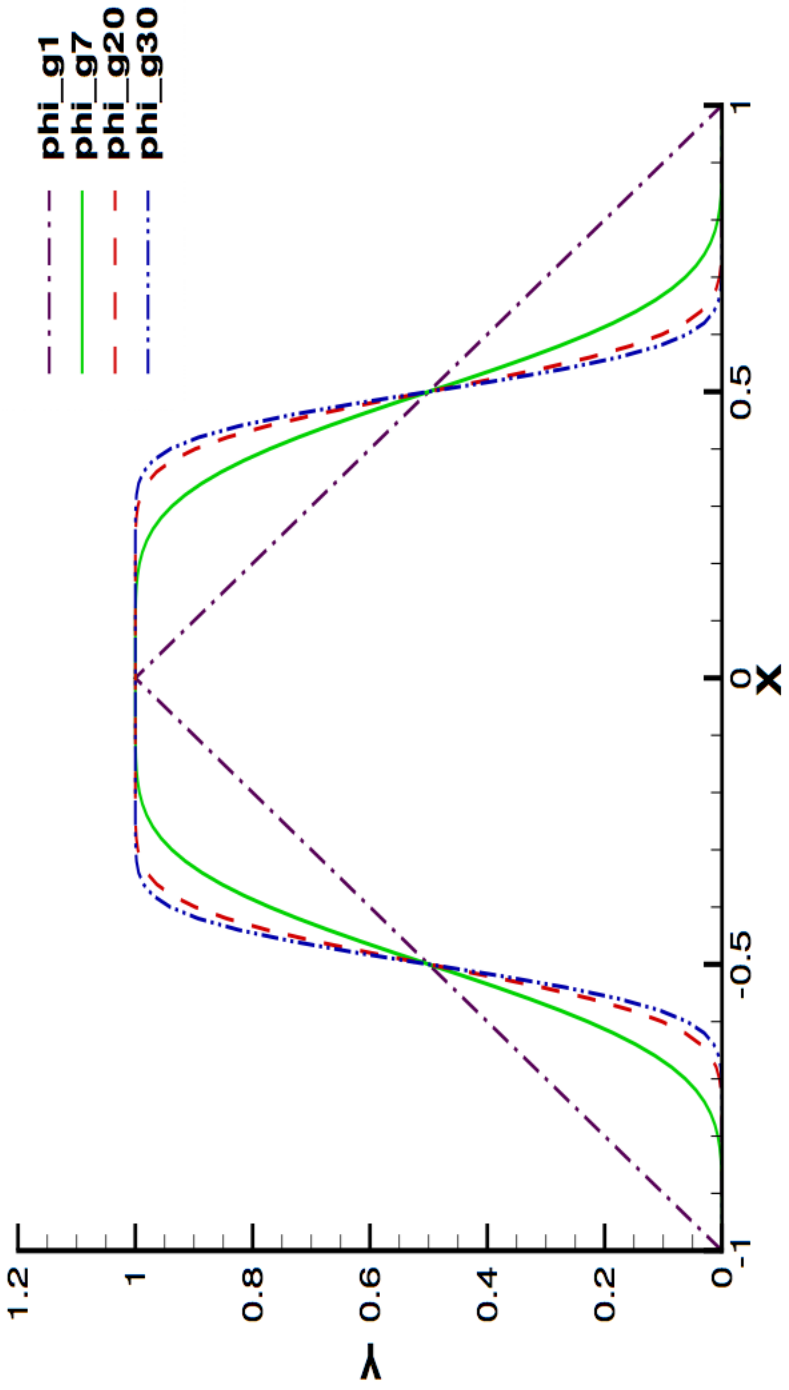

FIGURE 2: $\phi_{g_n}^{(pp)}$ for various $n = 1, 7, 20, 30$.

1. The second recurrence relation implies that $a_1^{(n)} = n$ for each n.

2. Using the recurrence relation (4), $g_n(x)$ is as follows:

$$\begin{aligned} g_1(x) &= 1 \\ g_2(x) &= 1 - 2x \\ g_3(x) &= 1 - 3x + 6x^2, \\ g_4(x) &= 1 - 4x + 10x^2 - 20x^3, \\ \vdots \quad & \quad \vdots \qquad\qquad \vdots \end{aligned}$$

   $\phi_{g_1}^{(pp)}, \phi_{g_7}^{(pp)}, \phi_{g_{20}}^{(pp)}$, and $\phi_{g_{30}}^{(pp)}$ that are $\mathcal{C}^0, \mathcal{C}^6, \mathcal{C}^{19}, \mathcal{C}^{29}$- functions. $\phi_{g_n}^{(pp)}$ for $n = 1, 7, 20, 30$ are depicted in Figure 2.

3. $\phi_{g_1}^{(pp)}$ is the hat function which is a $\mathcal{C}^0$-piecewise linear PU function. $\phi_{g_2}^{(pp)}$ is a $\mathcal{C}^1$-piecewise cubic polynomial PU function.

Lemma 1 *For all $n \geq 1$, $g_n(x)$ satisfies the following relation :*

$$n g_n(x) + (1 + x) g_n'(x) = (2n - 1) a_{n-1}^{(n)} (-x)^{n-1}, \tag{6}$$

Proof.

$$\begin{aligned} & n g_n(x) + (1 + x) g_n'(x) \\ &= n\big(1 + \sum_{k=1}^{n-1} (-1)^k a_k^{(n)} x^k\big) + \sum_{k=1}^{n-1} (-1)^k k a_k^{(n)} x^{k-1} + \sum_{k=1}^{n-1} (-1)^k k a_k^{(n)} x^k \\ &= n + \sum_{k=1}^{n-1} (-1)^k n a_k^{(n)} x^k + \sum_{k=0}^{n-2} (-1)^{k+1} (k+1) a_{k+1}^{(n)} x^k + \sum_{k=1}^{n-1} (-1)^k k a_k^{(n)} x^k \\ &= n - a_1^{(n)} + \sum_{k=1}^{n-2} \Big[(n + k) a_k^{(n)} - (k + 1) a_{k+1}^{(n)}\Big] (-x)^k + (2n - 1) a_{n-1}^{(n)} (-x)^{n-1} \\ &= (2n - 1) a_{n-1}^{(n)} (-x)^{n-1} \end{aligned}$$

□

By using the above lemma, we can prove the following.

Lemma 2 *For all $n \geq 1$, the function above, $g_n(x)$, satisfies the following relation:*

$$1 - x^n g_n(x-1) = (1-x)^n g_n(-x). \tag{7}$$

Proof. Let $F(x) = x^n g_n(x-1) + (1-x)^n g_n(-x) - 1$. Then, using Eqt. (6): $n g_n(x) + (1+x) g_n'(x) = (2n-1) a_{n-1}^{(n)} (-x)^{n-1}$, we have

$$\begin{aligned} F'(x) &= x^{n-1}(n g_n(x-1) + x g_n'(x-1)) - (1-x)^{n-1}(n g_n(-x) + (1-x) g_n'(-x)) \\ &= x^{n-1}((2n-1) a_{n-1}^{(n)} (1-x)^{n-1}) - (1-x)^{n-1}((2n-1) a_{n-1}^{(n)} x^{n-1}) = 0. \end{aligned}$$

Since $F(1) = 0$, $F(x) = 0$, which implies the lemma. □

The following theorem proves that the piecewise polynomial functions defined by expression (3) are indeed basic PU functions.

Theorem 1 *For all $n \geq 1$, the piecewise polynomial functions $\phi_{g_n}^{(pp)}$ defined by (3) satisfy the following.*

(i) $\phi_{g_n}^{(pp)}(x) \in \mathcal{C}^{n-1}(\mathbb{R})$,

(ii) $\phi_{g_n}^{(pp)}(x-1) + \phi_{g_n}^{(pp)}(x) + \phi_{g_n}^{(pp)}(x+1) = 1$ *for* $x \in (-1, 1)$,

(iii) *The degrees of the polynomial on each subinterval are* $(2n-1)$,

(iv) $\phi_{g_n}^{(pp)}(x)$ *is symmetric about the y-axis*,

(v) $\displaystyle\int_{\mathbb{R}} \phi_{g_n}^{(pp)}(x) dx = 1.$

Proof. (i), (iii), and (iv) are not difficult to show.

If $x \in [0, 1]$, then applying (7), we have the following:

$$\begin{aligned} \sum_{k \in \mathbb{Z}} \phi_{g_n}^{(pp)}(x-k) &= (1-x)^n g_n(-x) + x^n g_n(x-1) \\ &= \Big[1 - x^n g_n(x-1)\Big] + x^n g_n(x-1) = 1, \end{aligned}$$

which proves (ii).

Now let us prove (v).

$$\begin{aligned}\int_{-1}^{0}(1+x)^n g_n(x)dx &= \int_{0}^{1}(1-x)^n g_n(-x)dx \text{ (by the symmetry property)}\\ &= \int_{0}^{1}\Big[1-x^n g_n(x-1)\Big]dx \text{ (by Eqn. (7))}\\ &= \int_{0}^{1}1dx-\int_{0}^{1}x^n g_n(x-1)dx\end{aligned}$$

Thus,

$$\int_{-1}^{0}(1+x)^n g_n(x)dx+\int_{0}^{1}x^n g_n(x-1)dx=1.$$

By substitution: $x-1=-t$, the second integral becomes

$$\int_{0}^{1}x^n g_n(x-1)dx=\int_{0}^{1}(1-t)^n g_n(-t)dt.$$

This is the property (v). □

The converse of Theorem (1) is also true which implies the uniqueness.

Theorem 2 *If a piecewise polynomial $\psi(x)$ satisfies the following conditions:*

- (i) *$\psi(x)$ is symmetric about the y-axis.*
- (ii) *$\psi(x)$ is composed of exactly two polynomials of degree $2n-1$.*
- (iii) *$\psi(x)$ is a $\mathcal{C}^{n-1}-PU$ function.*
- (iv) *$\psi(0)=1$, and $supp(\psi(x))=[-1,1]$.*

then

$$\psi(x)=\phi_{g_n}^{(pp)}.$$

Proof. Since $\psi(x)$ is symmetric, it is sufficient to investigate only $\psi^+(x)$. $\psi^+(x)$ is the restriction of $\psi(x)$ onto $[0,1]$. Because $\psi(x)$ is a PU function,

$$\psi(x+1)+\psi(x)+\psi(x-1)=1, \text{ for } x\in[-1,1].$$

Moreover, $\psi(x) \in \mathcal{C}^{n-1}(\mathbb{R})$, we have the following:

$$\begin{aligned} \frac{d^j \psi(x)}{dx^j}|_{x=0} &= 0, \text{ for } j = 1, \cdots, n-1, \\ \psi(x)|_{x=0} &= 1, \\ \psi^+(x) &= (1-x)^n (b_0 + b_1 x + b_2 x^2 + \cdots + b_{n-1} x^{n-1}). \end{aligned}$$

Consider the difference of two functions:

$$\begin{aligned} G(x) &= (1-x)^n g_n(-x) - \psi^+(x) \\ &= (1-x)^n [(a_0^{(n)} - b_0) + (a_1^{(n)} - b_1)x + \cdots + (a_{n-1}^{(n)} - b_{n-1})x^{n-1}] \end{aligned}$$

Then, we have

$$G(0) = G'(0) = G''(0) \cdots = G^{(n-1)}(0) = 0,$$

which implies that

$$\psi^+(x) = (1-x)^n g_n(-x), \text{ for all } x \in [0,1].$$

□

Remark *The gradient of the scaled basic PU function is bounded as follows:*

$$\frac{d}{dx}\left[\phi_{g_n}^{(pp)}(\frac{x}{2\delta})\right] \leq \frac{C}{\delta} \tag{8}$$

Whenever $n \leq 3$ the constant $C \approx 1$. Detailed proof is given in (Oh et al., 2008).

If there is no flat-top region in the partition of unity shape function, it is well known that the resulting stiffness matrix has a large condition number. Note $\phi_{g_n}^{(pp)}$ does not have a flat top region for small n (Figure 1) but as n gets larger one can observe $\phi_{g_n}^{(pp)}$ starts to become flat near the center (Figure 2). However, a large n makes the gradient of $\phi_{g_n}^{(pp)}$ bigger and could cause instability. A simple modification of the two piece polynomial partition of unity shape function $\phi_{g_n}^{(pp)}$ can result in a wide flat-top region.

Now we define a three piece polynomial PU function with a wide flat-top that has compact support in the following way.

Definition *For integers $n \geq 1$, we define a piecewise polynomial function $\psi_{[a,b]}^{(\delta,n-1)}(x)$ as follows:*

$$\psi_{[a,b]}^{(\delta,n-1)}(x) = \begin{cases} \phi_{g_n}^L(\frac{x-(a+\delta)}{2\delta}) & if \quad x \in [a-\delta, a+\delta] \\ 1 & if \quad x \in [a+\delta, b-\delta] \\ \phi_{g_n}^R(\frac{x-(b-\delta)}{2\delta}) & if \quad x \in [b-\delta, b+\delta] \\ 0 & if \quad x \notin [a-\delta, b+\delta]. \end{cases} \tag{9}$$

where $\delta \leq (b-a)/3$, $\phi_{g_n}^L(x) := (1+x)^n g_n(x)$, and $\phi_{g_n}^R(x) := (1-x)^n g_n(-x)$.

Figure 3 shows $\psi_{[-1,1]}^{(0.15,2)}(x)$ and its derivative $\frac{d}{dx}\psi_{[-1,1]}^{(0.15,2)}(x)$. Note the wide flat-top region in the partition of unity shape function. It is also important to see that the derivative of $\psi_{[-1,1]}^{(0.15,2)}(x)$ is also smooth. In fact, $\psi_{[-1,1]}^{(0.15,2)}(x)$ is a C^2 function. The above definition is an extension of a two-piece polynomial shape function that was first introduced by Oh et al. (2008). It can be shown that the partition of unity shape function $\psi_{[a,b]}^{(\delta,n-1)}(x)$ is a special case of the convolution partition of unity when a scaled conical window function (1) is used for the convolution. The definition of *convolution partition of unity* follows.

Definition *Let $Q_k = (x_k, x_{k+1})$ be an interval with $|x_{k+1} - x_k| \geq 3\delta$ and the characteristic function of Q_k is defined by*

$$\chi_{Q_k}(x) = \begin{cases} 1, & if\ x \in Q_k, \\ 0, & if\ x \notin Q_k. \end{cases} \tag{10}$$

The convolution PU function of χ_{Q_k} and $w_\delta^{(l)}$ is defined by

$$\begin{aligned}
\psi_k^{(\delta,l)}(x) &= \int_{\mathbb{R}} w_\delta^{(l)}(x-y)\chi_{Q_k}(y)dy = \int_{Q_k} w_\delta^{(l)}(x-y)dy \\
&= \begin{cases}
f_{k+1}(x) = \displaystyle\int_{x-x_{k+1}}^{\delta} w_\delta^{(l)}(t)dt, & \text{if } x \in [x_{k+1}-\delta, x_{k+1}+\delta], \\
1, & \text{if } x \in [x_k+\delta, x_{k+1}-\delta], \\
f_k(x) = \displaystyle\int_{-\delta}^{x-x_k} w_\delta^{(l)}(t)dt, & \text{if } x \in [x_k-\delta, x_k+\delta], \\
0, & \text{if } x \in \mathbb{R}\backslash[x_k-\delta, x_{k+1}+\delta].
\end{cases}
\end{aligned} \tag{11}$$

Since the scaled window function is a polynomial, $\psi_k^{(\delta,l)}(x)$ becomes a piecewise polynomial. In fact, $\psi_{[a,b]}^{(\delta,n-1)}(x)$ is the convolution, $\chi_{[a,b]}(x) * w_\delta^{n-1}(x)$, of the characteristic function $\chi_{[a,b]}$, and the scaled window function w_δ^{n-1}, defined by (1).

Although the convolution partition of unity is very useful, especially in constructing non-rectangular patch partition of unity in 2D, it is numerically inefficient, and it is not easy to extend the two dimensional construction of the convolution PU functions to the three-dimensional case. An obvious choice for higher dimensional PU functions is the tensor product of one dimensional PU functions. The tensor product of these one-dimensional PU functions yields higher dimensional PU functions with a flat-top. Although this simple extension works well with rectangles(2D) and cubes(3D), using tensor products one cannot make neither triangular, general quadrangular patches (2D), nor tetrahedral, pentahedral, general hexaheral patches, arising in background meshes for meshless methods. Until very recently (Oh et al., 2009) closed form smooth PU functions for general polygonal patches (2D) and general polyhedral patches (3D) have not been available. So the only way to handle complicated mesh structure was using the convolution partition of unity (Oh and Jeong, 2009).

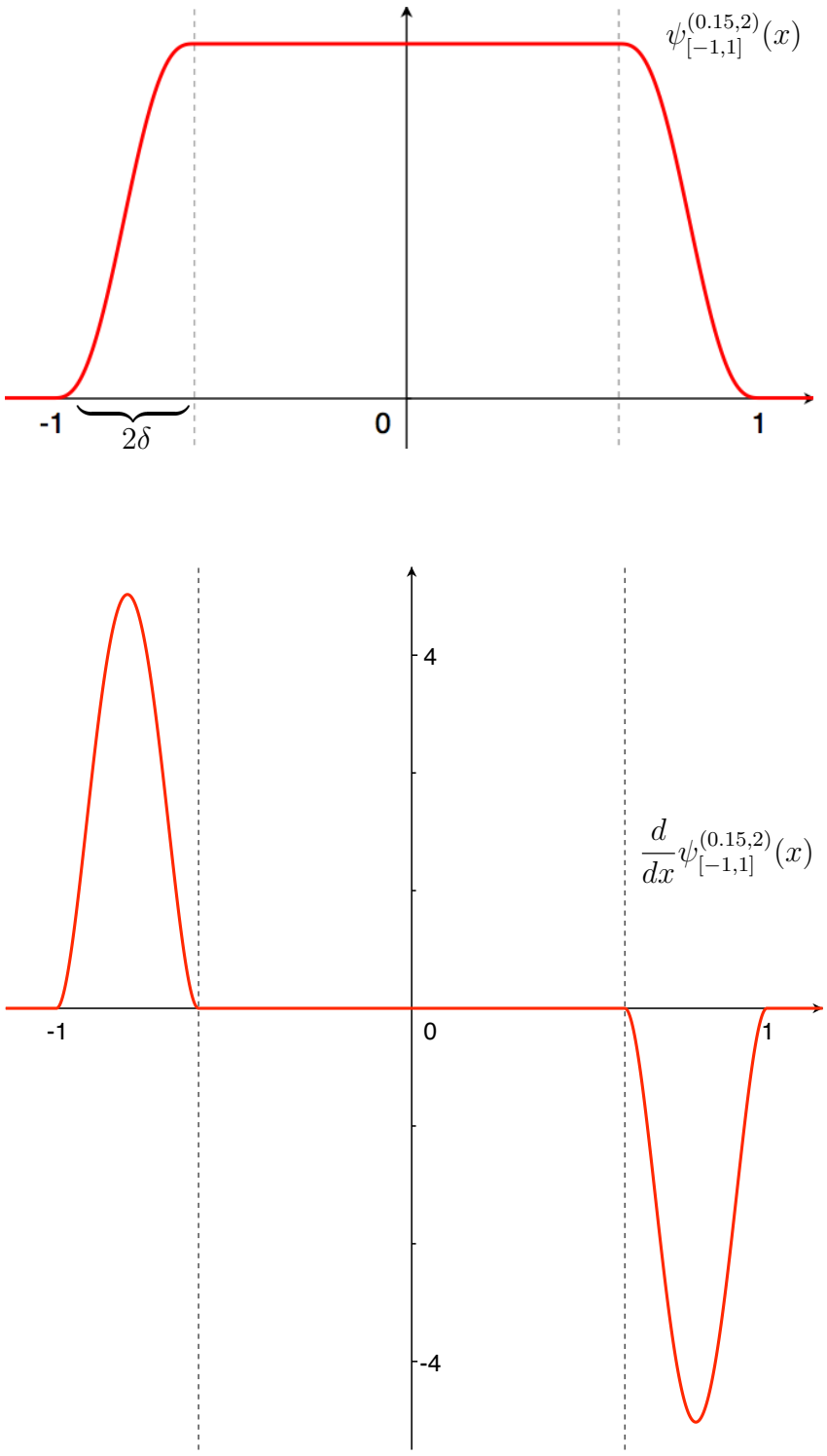

FIGURE 3: Three piece polynomial C^n partition of unity function, $\psi^{(\delta,n-1)}_{[a,b]}$.

[D] The product partition of unity

Oh et al. (2009) introduced a simple unified method named **the generalized product method** to construct *smooth closed form partition of unity functions for general polygonal patches (2D) and polyhedral patches (3D).* In the following, we give a brief description of the method.

Note that the two functions $\phi^R_{g_n}, \phi^L_{g_n}$, defined by (9), satisfy the following relation:

$$\phi^R_{g_n}(\xi) + \phi^L_{g_n}(\xi - 1) = 1, \text{ for } \xi \in [0, 1]. \tag{12}$$

Hence, if $\varphi : [-\delta, \delta] \to [0, 1]$ is defined by

$$\varphi(x) = (x + \delta)/(2\delta),$$

then we have

$$\phi^R_{g_n}(\varphi(x)) + \phi^L_{g_n}(\varphi(x) - 1) = 1, \text{ for } x \in [-\delta, \delta].$$

Using the latter equation gives two basic one-dimensional $\mathcal{C}^{n-1}$ functions

$$\psi^R_0(x) = \begin{cases} 1 & \text{if } \ x \le -\delta \\ \phi^R_{g_n}(\frac{x+\delta}{2\delta}) & \text{if } \ x \in [-\delta, \delta] \\ 0 & \text{if } \ x \ge \delta, \end{cases} \tag{13}$$

$$\psi^L_0(x) = \begin{cases} \phi^L_{g_n}(\frac{x-\delta}{2\delta}) & \text{if } \ x \in [-\delta, \delta] \\ 1 & \text{if } \ x \ge \delta, \\ 0 & \text{if } \ x \le -\delta. \end{cases} \tag{14}$$

such that

$$0 \le \psi^L_0(x), \psi^R_0(x) \le 1, \quad \psi^R_0(x) + \psi^L_0(x) = 1, \text{ for all } x \in \mathbb{R}. \tag{15}$$

Note that the support of these two functions are unbounded.

Two **basic two-dimensional $\mathcal{C}^{n-1}$-PU functions** are defined by

$$\Psi^R(x,y) = \psi_0^R(x) \text{ and } \Psi^L(x,y) = \psi_0^L(x), \text{ for all } (x,y) \in \mathbb{R}^2. \tag{16}$$

such that $\Psi^R(x,y) + \Psi^L(x,y) = 1$, for all $(x,y) \in \mathbb{R}^2$.

Remark *In other words, two functions $\Psi^R(x,y)$ and $\Psi^L(x,y)$ are the compositions of the coordinate projections with (13) and (14), respectively.*

Suppose a domain Ω is partitioned into the m-number of **convex** subregions $Q_1, \cdots, Q_m$, by n-number of straight lines, rays, or broken lines $L_1, \cdots, L_n$ so that, for each $j = 1, \cdots, m$, $Q_j^{\text{flat}} = \{(x,y) \in Q_j | \text{dist}((x,y), L_k) > \delta, k = 1, \cdots, n\}$, the flat-top part of Q_j, has a positive measure. We assume the following rules and definitions:

1. At each vertex of the partition, no more than two lines or rays can intersect. Exceptions are explained in (Oh et al., 2009). Only five cases and their combinations are allowed.

2. The orientations of lines are as usual: the right end of a line is the positive side. For $k = 1, \cdots, n$, φ_k is an affine mapping on $\mathbb{R}^2$ that maps the line L_k onto the y-axis so that orientations can be matched. We define two basic PU functions by

$$\Psi_k^R = \Psi^R \circ \varphi_k \text{ and } \Psi_k^L = \Psi^L \circ \varphi_k, \quad \text{for each } k = 1, \cdots, n. \tag{17}$$

3. Suppose for each j, the patch Q_j is surrounded by the lines $L_{j1}, \cdots, L_{j\alpha}$. Then by (17), two basic PU functions correspond to each of these α lines. Define Ψ_j^P by the product of those basic PU functions among 2α basic PU functions that are one on Q_j^{flat}.

Then we have the following:

- $\{\Psi_j^P : j = 1, \cdots, m\}$ is a partition of unity for the domain Ω ;
- The flat-top subregion of the support of Ψ_j^P is Q_j^{flat}. The PU function Ψ_j^P is the product of the same number of basic PU functions as the number of lines surrounding the patch Q_j that are not the boundary lines of Ω (the basic PU functions are not needed for the boundary lines of the polygonal domain Ω).
- Even though the partitioning lines are broken the above rule for the construction of the product PU function holds. Details can be found in (Oh et al., 2009).

Definition *We denote the PU function Ψ_j^P that is the product of basic PU functions corresponding to lines surrounding the patch Q_j as* **the product partition of unity function.**

The product partition of unity functions corresponding to a nonconvex patch, a triangular patch, and a quadrangular patch are depicted in Figures 4 and 5. We refer to (Oh et al., 2009) for more examples and the details.

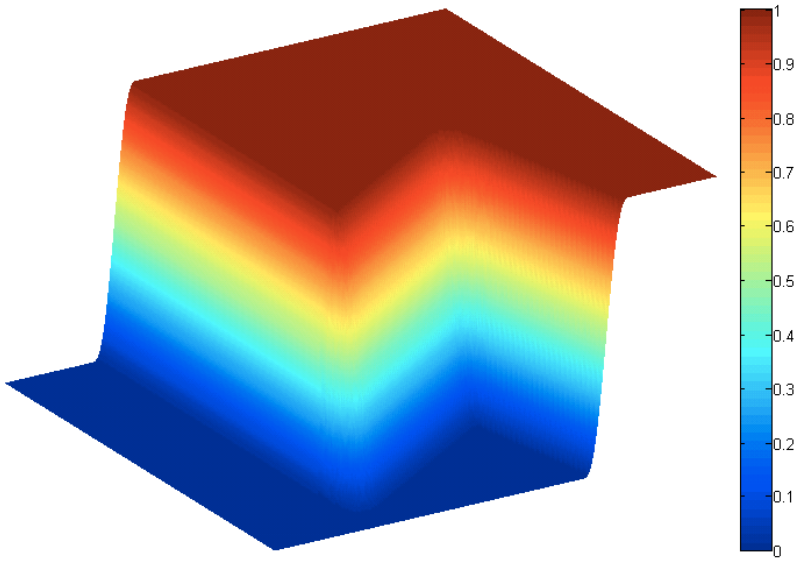

FIGURE 4: Generalized product PU functions for a nonconvex patch.

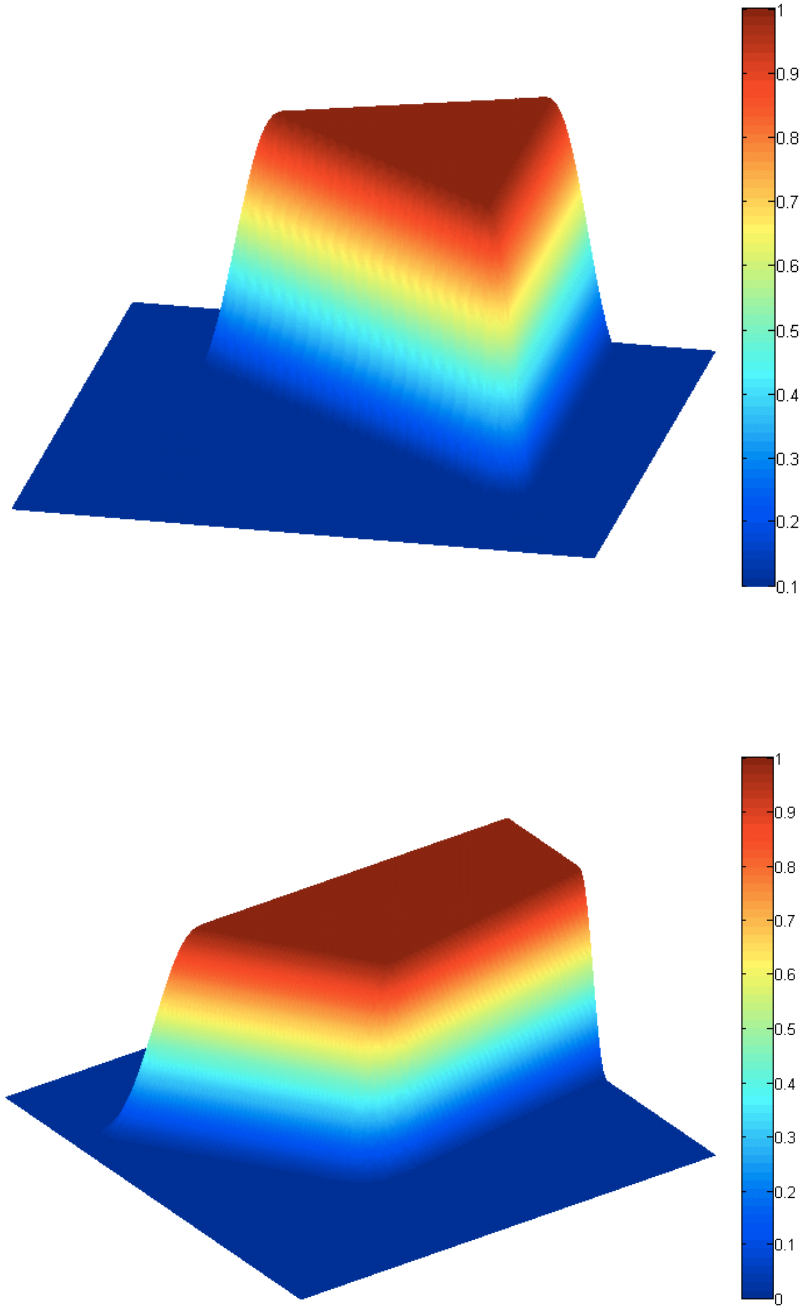

FIGURE 5: Generalized product PU functions for polygonal patches.

1.4 Generalized Finite Element Method

In the previous section, we introduced the RPP shape functions *with compact support* corresponding to the uniformly distributed particles. In the cases when the RPP shape functions associated with uniformly distributed particles are used for basis functions in a Galerkin approximation, we do not need any mesh at all. However, if the problem domain Ω is not as simple as a rectangle, it is hard to distribute particles uniformly into Ω. Thus, if Ω is a non-rectangular polygon, we divide Ω into quadrangular patches $Q_J, J = 1, \cdots, N$. Then, on each patch Q_J, we can plant particles so that they can be uniformly distributed through a patch mapping from a reference square to a quadrangle. Then the RPP shape functions can be constructed on each patch. Next, the locally defined RPP shape functions are connected together by using partition of unity associated with patches $Q_1, Q_2, \cdots, Q_N$. In this section, we present the meshless method that uses the background mesh $Q_1, Q_2, \cdots, Q_N$.

Let us consider the following second order elliptic equation

$$\begin{cases} -\Delta u &= f \text{ in } \Omega, \\ u &= u_d \text{ on } \Gamma_D, \\ \frac{\partial u}{\partial n} &= u_n \text{ on } \Gamma_N, \end{cases} \tag{18}$$

where Ω is a polygonal domain, $\mathbf{n}$ is the outward normal vector along $\partial\Omega$ and $\Gamma_D \cup \Gamma_N = \partial\Omega$. Then the corresponding variational equation is:
Find $u \in H^1(\Omega)$ such that $u = u_d$ on Γ_D and

$$\mathcal{B}(u, v) \equiv \int_\Omega \nabla u \cdot \nabla v - \int_{\Gamma_D} v \nabla u \cdot \mathbf{n} = \int_\Omega f v + \int_{\Gamma_N} u_n v \equiv \mathcal{F}(v), \tag{19}$$

for all $v \in H^1_D(\Omega)$.

Now, the *Generalized Finite Element Method* for a numerical solution to this model problem is described as follows:

1. (*Generate Background Mesh*) To construct PU functions with flat-top and highly

smooth local approximation functions for numerical solutions of (19), the domain Ω is partitioned into polygonal patches. Typically we use triangular or quadrangular patches for convenience. Unlike the conventional FEM mesh, the background mesh is flexible. For example, we allow the hanging nodes and pentagonal patches.

2. (*Construct partition of unity functions with a flat-top*) For $J = 1, 2, \ldots, M$, let Ψ_J be the PU function with flat-top corresponding to the patches Q_J and ω_J be the support of Ψ_J.

3. (*Planting particles*) Let Q^t be the reference triangular patch and Q^r be the reference rectangular patch. Suppose $\hat{p}_k, \quad k = 1, 2, \cdots, N$, are arbitrary (or uniformly) distributed particles on the reference patches. Let $\phi_J^t : Q^t \to \omega_J$ (if the physical patch is triangular) or $\phi_J^q : Q^r \to \omega_J$ (if the physical patch is quadrangular) be the patch mappings. Then, through the patch mappings ϕ_J^t or ϕ_J^q, we have particles $p_{Jk} = (\phi_J^{t \text{ or } q})^{-1}(\hat{p}_k)$, $k = 1, \cdots, N_J$ that are distributed uniformly or non-uniformly in ω_J.

4. (*Local approximation functions*) Suppose $\hat{g}_k \ k = 1, \cdots, \hat{N}$ are smooth RPP shape functions corresponding to the particles planted in the reference patch that satisfy the Kronecker delta property. Then these RPP shape functions on the reference patch can be used to build local approximation functions on the support w_J of the physical patch Q_J as follows:

$$g_{Jk} = \hat{g}_k \circ (\phi_J^q)^{-1} (\text{or } \hat{g}_k \circ (\phi_J^t)^{-1}), \quad k = 1, \cdots, N_J. \tag{20}$$

For example, we can use the tensor product of Lagrange interpolation functions corresponding to arbitrarily spaced N_x numbers of nodes in the x-direction and those corresponding to arbitrarily spaced N_y numbers of nodes in the y-direction. These are RPP shape functions and satisfy the Kronecker delta prop-

erty. In other words, let $L_{n,j}(x)$ be the j-th Lagrange interpolation polynomial of degree $(n-1)$ associated with n distinct nodes $x_1, \cdots, x_n$ in $[0,1]$, defined by

$$L_{n,j}(x) = \frac{\prod_{k=1,k\neq j}^{n}(x-x_k)}{\prod_{k=1,k\neq j}^{n}(x_j-x_k)}.$$

Then $g_{Jk}(x,y) = L_{n,l}(x) \times L_{n,m}(y); 1 \leq l,m \leq n, k = n(l-1)+m$ are RPP shape functions with polynomial reproducing order $n-1$.

5. (*Smooth Global RPP basis functions*) The global approximation functions with compact support are constructed as follows:

$$\Phi_{Jk}(x,y) = \Psi_J(x,y) \cdot g_{Jk}(x,y), \quad J = 1, \cdots, M; k = 1, \cdots, N_J. \tag{21}$$

These global approximation functions are **highly smooth** and correspond to the particles:

$$p_{Jk}, \quad J = 1, 2, \cdots, M; \quad k = 1, 2, \cdots, N_J.$$

We also assume that each set $\{g_{Jk} : k = 1, \cdots, N_J\}$, of local approximation functions has the polynomial reproducing property and satisfies the Kronecker delta property at the particles planted on ω_J.

6. (*GFEM approximation space*) The vector space spanned by those approximation functions defined by (21), denoted by V^{gfem}, is said to be the GFEM approximation space.

The Galerkin approximation method with use of this GFEM approximation space V^{gfem} is said to be the **Generalized Finite Element Method.** The GFEM approximation can be written as

$$u^{\text{gfem}}(x,y) = \sum_J \sum_k c_{Jk} \cdot G_{Jk}(x,y) = \sum_J \Psi_J(x,y) \left[\sum_k c_{Jk} \cdot g_{Jk}(x,y) \right]. \tag{22}$$

1.5 Basis Enrichment

There are many different choices for the local approximation functions. Some of them can be found in (Oh et al., 2008). It is important to understand this flexibility of selecting local approximation functions is one of the most powerful aspect of partition of unity finite element methods.

In the following chapters, we will use singular functions or special functions that mimic the behavior of the singularity on certain patch(es) and on the rest of the patches, Lagrange interpolation polynomials will be used as local approximation functions. In cases where a special function is used, the numerical integration is not exact. The optimal choice of local approximation spaces is discussed extensively in (Babuska et al., 2002).

As pointed out earlier, the flexibility to choose a local approximation space enables us to add special functions to approximation spaces. Enrichment means adding some special functions to the sets of existing local approximation functions in the following way.

Definition *The Enriched Generalized Finite Element approximation space* V^{enrich} *is defined as follows: Suppose we want to enrich local approximation functions on the patches*

$$Q_{J_1}, Q_{J_2}, \cdots, Q_{J_s}$$

with sets of special functions:

$$\sigma_{J_i,k}, \quad k = 1, 2, \cdots, N_{J_i} \text{ for } i = 1, 2, \cdots, s.$$

Then V^{enrich} *is the vector space spanned by,*

$$V^{\text{gfem}} \cup \{\Psi_{J_i}\sigma_{J_i k} : k = 1, 2, \cdots, N_{J_i}, i = 1, 2, \cdots, s\}.$$

The Galerkin approximation for the second order elliptic equation with the bound-

ary condition (18) associated with the Enriched Generalized Finite Element approximation space V^{enrich} is as follows : Find

$$u^{\text{enrich}} = \sum_{J=1}^{M} \left[\sum_{k=1}^{N_J} c_{Jk} \Psi_J g_{Jk} \right] + \sum_{i=1}^{s} \left[\sum_{l=1}^{N_{J_i}} d_{J_i,l} \Psi_{J_i} \phi_{J_i,l} \right]. \tag{23}$$

such that

$$\mathcal{B}(u^{\text{enrich}}, v) \;=\; \mathcal{F}(v), \quad \text{for } v \in V^{\text{enrich}}, \tag{24}$$

where $\mathcal{B}$ and $\mathcal{F}$ are defined as (19).

Calculation of a stiffness matrix involves the following integration.

$$\int_{\omega_J \cap \omega_L} \nabla(v_{J,i})^T \cdot \nabla(v_{L,j}) d\Omega \tag{25}$$

where J, L indicates the patch number and $\nabla = (\frac{\partial}{\partial x}, \frac{\partial}{\partial y})^T$. Also $v_{J,i}, v_{L,j} \in V^{\text{enrich}}$. Also the components of the load vector is the following.

$$\int_{\omega_J \cap \omega_L} f \cdot v_{J,k} d\Omega. \tag{26}$$

Remark *Since the PU function Ψ is piecewise polynomial, if the local approximation functions are chosen as polynomials. Then the integration (25) can be calculated exactly. Note the integrations (25) and (26) could be difficult whenever the enriched functions are singular.*

The integration (25) have four different types :

$$\int_{\omega_J \cap \omega_L} \nabla(\Psi_J \cdot g_{Jk})^T \cdot \nabla(\Psi_L \cdot g_{Ll}) d\Omega, \tag{27}$$

$$\int_{\omega_J \cap \omega_L} \nabla(\Psi_J \cdot g_{Jk})^T \cdot \nabla(\Psi_L \cdot \phi_{Ll}) d\Omega, \tag{28}$$

$$\int_{\omega_J \cap \omega_L} \nabla(\Psi_J \cdot \phi_{Jk})^T \cdot \nabla(\Psi_L \cdot g_{Lk}) d\Omega, \tag{29}$$

$$\int_{\omega_J \cap \omega_L} \nabla(\Psi_J \cdot \phi_{Jk})^T \cdot \nabla(\Psi_L \cdot \phi_{Ll}) d\Omega. \tag{30}$$

where g is a RPP approximation function and ϕ is a singular function for enrichment.

1.6 Error Estimate

The error estimate of GFEM can be found in several different forms. The following theorem can be found in Oh and Jeong (2009).

Theorem 3 *Let Ω be a 2D convex polygon. Also let $\{\Psi_J(x,y) : J = 1, 2, \cdots, N\}$ be a partition of unity corresponding to the patch $\{Q_J : J = 1, 2, \cdots, N\}$ of Ω. Also denote Q_J^{flat} for the flat-top region of $\Psi_J(x,y)$. Assume there exists a positive integer M such that for every $x \in \Omega$, $card\{J : x \in \omega_J\} \leq M$, where $\omega_J = supp(\Psi_J)$. Let a collection of local approximation spaces $V_J \subset H^1(\Omega \cap \omega_J)$ be given on each patch Q_J. Let us assume the local approximation space V_J has the following approximation properties on each patch Q_J :*

The function $u \in H^1(\Omega)$ can be approximated by a function $g_J \in V_J$ such that

1. $||u - g_J||_{L^2(\Omega \cap w_J)} \leq \epsilon_J^{(0)}$,
2. $||u - g_J||_{L^2(\Omega \cap (\omega_J \setminus \omega_J^{\text{flat}}))} \leq \epsilon_{J,\text{non-flat}}^{(0)}$,
3. $||\nabla(u - g_J)||_{L^2(\Omega \cap w_J)} \leq \epsilon_J^{(1)}$,

for all $J = 1, 2, \cdots, N$. Then ,

$$u^{\text{gfem}} = \sum_{J=1}^{N} \Psi_J \cdot g_J$$

satisfies the following global estimates.

$$||u - u^{\text{gfem}}||_{L^2(\Omega)}^2 \leq M(\sum_{J=1}^{N} (\epsilon_J^{(0)})^2) \tag{31}$$

and

$$||\nabla(u - u^{\text{gfem}})||_{L^2(\Omega)}^2 \leq 2M(\sum_{J=1}^{N} (\frac{C_\nabla}{\delta})^2 (\epsilon_{J,\text{non-flat}}^{(0)})^2 + (\epsilon_J^{(1)})^2) \tag{32}$$

where C_∇ is a constant independent of δ.

CHAPTER 2: THE MOTZ PROBLEM

2.1 Introduction

The Motz problem was first introduced by Motz (Motz, 1947). Since it was introduced the Motz problem has served as a benchmark problem to verify the efficiency of numerical methods in the presence of boundary singularities. The Motz problem is a Laplace equation with mixed Neumann-Dirichlet boundary conditions as follows:

$$\begin{cases} -\Delta u &= 0 \text{ in } \Omega = \{(x,y) | -1 < x < 1, 0 < y < 1\} \\ u &= 0 \text{ on } \Gamma_1, \\ u &= 500 \text{ on } \Gamma_2, \\ \frac{\partial u}{\partial n} &= 0 \text{ at } \Gamma \setminus (\Gamma_1 \cup \Gamma_2) \end{cases} \tag{33}$$

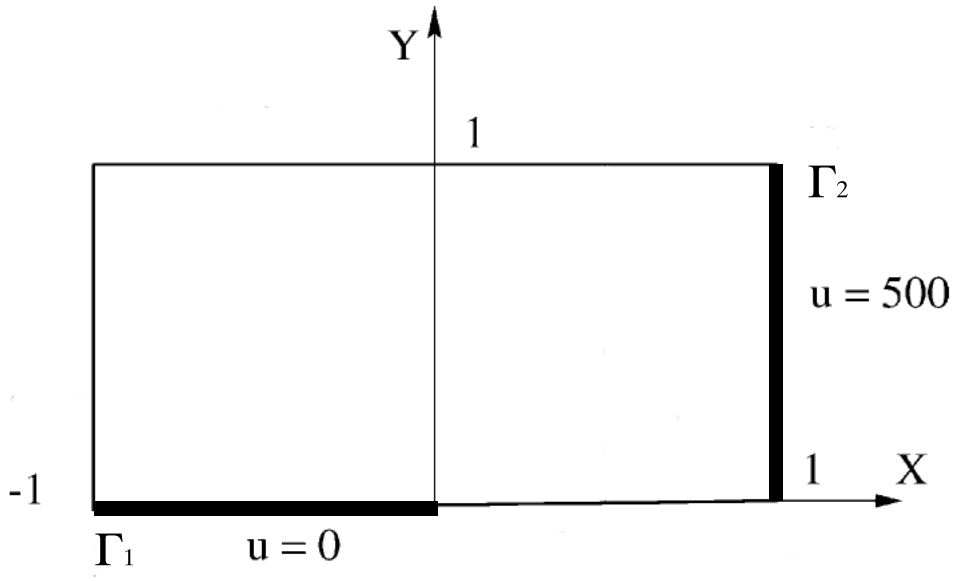

FIGURE 6: The Motz Problem.

Remark *The Motz problem has a jump boundary data singularity at the origin* $(0,0)$ *where the Neumann boundary condition and the Dirichlet boundary condition meet.*

The asymptotic solution of (33) can be expressed as an infinite series :

$$u(r,\theta) = \sum_{i=0}^{\infty} d_i r^{i+\frac{1}{2}} cos(i+\frac{1}{2})\theta. \tag{34}$$

Therefore, for an approximate solution of the Motz problem, we consider the partial sum of (34):

$$u_N(r,\theta) = \sum_{i=0}^{N} \tilde{d}_i r^{i+\frac{1}{2}} \cos(i+\frac{1}{2})\theta. \tag{35}$$

On the other hand, the exact solution of the Motz problem is available byconformal mapping methods (Rosser and Papamichael, 1975). They also obtained highly accurate approximations up to the first 20 coefficients.

Remark *The functions* $r^{i+\frac{1}{2}} \cos(i+\frac{1}{2})\theta$ *for each* i *satisfies the Dirichlet boundary condition along the negative* x*-axis and the Neumann condition along the positive* x*-axis.*

Special finite difference methods (J.R.Whiteman, 1971) and global element methods (Hendry and Delves, 1979, Kermode et al., 1985) were introduced to determine the singular coefficients $\tilde{d}_i$. Other methods such as one-zone blending (Morley, 1973), combination of two-zone blended singular basis functions (Wait and Mitchell, 1971), Boundary methods (Li et al., 1987), the method of auxiliary mapping (MAM) and mesh refinement (Lucas and Oh, 1993) are available for this problem, however approximations for the actual values $\tilde{d}_i$ were not available at all or were unsatisfactory. On the other hand, a finite difference approach (Wigley, 1988) as well as collocation trefftz method (Lu et al., 2004) successfully estimated the first several coefficients. Especially, the collocation trefftz method gives the highly accurate leading coefficient for the Motz problem.

2.2 Implementation

For an approximate solution of (33), Ω is partitioned into 39 patches as shown in Figure 7: 38 rectangular patches along the boundary and one rectangular patch containing the singularity. We will call the big center patch an **enriched patch** where singular functions are used as local approximation functions. On the remaining 38 small patches, the RPP local approximation functions defined by (21) are used. Note that the oscillatory behavior of the singular functions $r^{i+\frac{1}{2}}\cos(i+\frac{1}{2})\theta$ increases as i increases. Hence, to take account of this fact in the numerical integration, one would need to split the domain of integral into many smaller pieces. Note as the number of singular functions used as enrichment functions increases, so does the number of subdivisions in order to obtain accurate results. For a good numerical integration, the enriched patch is divided in the angular direction as well as the radial direction. In this dissertation, in terms of polar coordinate, the θ-direction was subdivided into 32 pieces and the r-direction is divided into two pieces to work with 40 singular functions, $r^{k+\frac{1}{2}}\cos(k+\frac{1}{2})\theta, k = 0, \cdots, 39$, for local approximation functions.

Two PU functions corresponding to two neighboring patches may have overlapping supports. The overlapping parts are strips of 2δ-width. In the following numerical computation, we use $\delta = 0.01$. In Figure 7, the thin strips represent the overlapping regions. Except on the overlapping regions, PU functions have a flat top on each patch, which implies the linear independence of the local approximation functions. In other words, PU functions with flat-tops make the condition number of the stiffness matrix reasonably small.

Remark *It is important to note that the partition of unity that is utilized in this example allows hanging nodes in background mesh; whereas hanging nodes are not allowed in the conventional finite element method. This is one of the advantages of the GFEM. The best way to handle singularity problems by the conventional FEM is by using adaptive mesh refinement. Since hanging nodes are not allowed, the mesh*

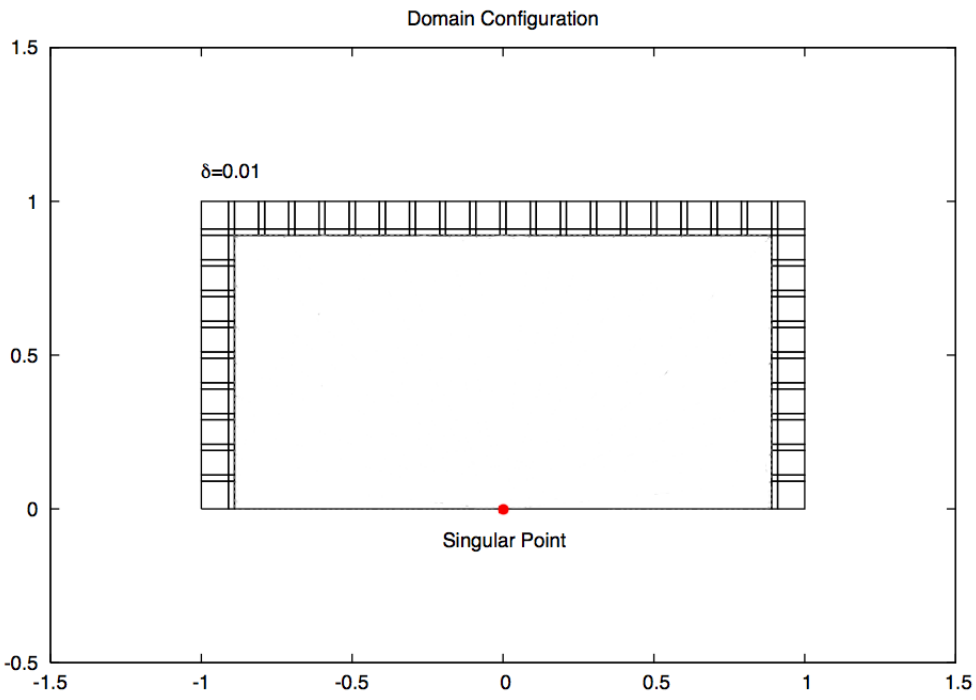

FIGURE 7: Partition of Unity.

should be globally refined. i.e. to avoid hanging nodes, there needs to be some extra work done to refine the mesh, and the degrees of freedom are increased by this mesh refinement. Moreover, if the singularity is strong, the convergence could be slow even if the mesh becomes extremely fine (Lucas and Oh, 1993).

Special attention is needed for numerical integration (28) − (30) on the enriched patch. Since all local approximation functions on the enriched patch are singular functions, we do not have the integration (27) on the enriched patch. On the other hand, at first glance, (28) and (29) seem to have problems because these have singular integrands. However, these integrations do not cause any trouble due to the fact that the integration is only performed on overlapping regions with 2δ of width near the boundary of the patch. Since the overlapping region is far away from the singular point $(0, 0)$, the integrands are not singular. The numerical integration may not be exact. Nevertheless, it can be treated well with a reasonable number of Gauss

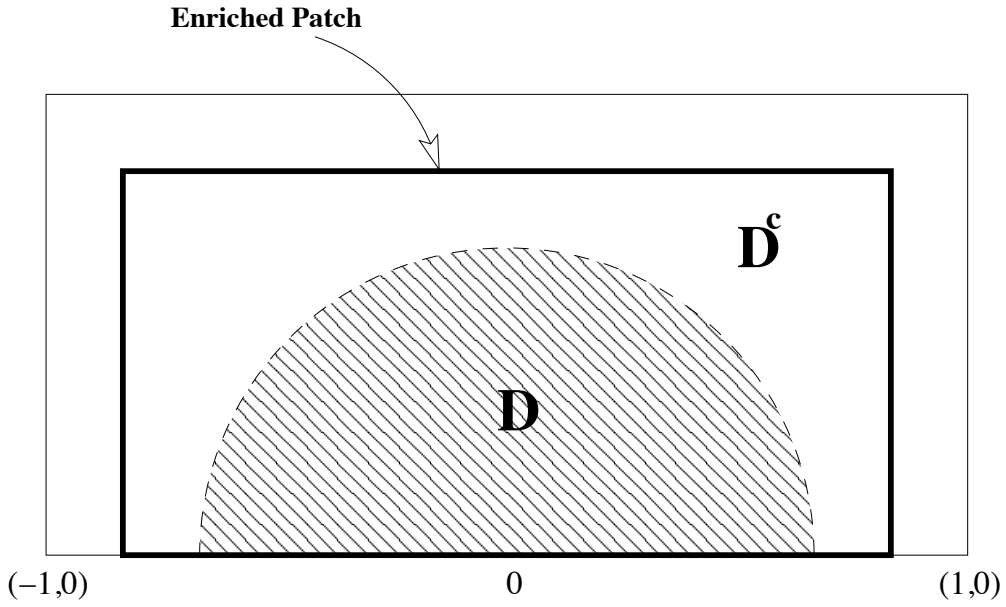

FIGURE 8: Region D and D^c.

points. Now integration (30) is the only integral left to consider. The following theorem shows the boundness of (30). It also gives an idea of how to get an accurate numerical integration.

Theorem 4

$$\int_{\Omega_{flat}} (\nabla_{x,y} g_i(r,\theta))^T (\nabla_{x,y} g_j(r,\theta))\, dxdy$$
$$= \left(\frac{1}{2}+i\right)\left(\frac{1}{2}+j\right) \int_{\Omega_{flat}} r^{i+j} \cos\left((i-j)\,\theta\right)\, drd\theta,$$

where Ω_{flat} denotes the flat top region of the PU function corresponding to the enriched patch shown in Figure 8, and $g_k(r,\theta) = r^{k+\frac{1}{2}} \cos((k+\frac{1}{2})\theta)$.

Proof. By a coordinate transformation, the gradient operator is transformed as follows:

$$\nabla_{x,y} = \begin{pmatrix} \dfrac{\partial}{\partial x} \\ \dfrac{\partial}{\partial x} \end{pmatrix} = \begin{pmatrix} \cos\theta & -\dfrac{1}{r}\sin\theta \\ \sin\theta & \dfrac{1}{r}\cos\theta \end{pmatrix} \nabla_{r,\theta} = \mathrm{M} \begin{pmatrix} \dfrac{\partial}{\partial r} \\ \dfrac{\partial}{\partial \theta} \end{pmatrix},$$

where $M = \begin{pmatrix} \cos\theta & -\frac{1}{r}\sin\theta \\ \sin\theta & \frac{1}{r}\cos\theta \end{pmatrix}$. For simplicity, we suppress (r,θ) in $g(r,\theta)$. Then,

$$\begin{aligned}
&\int_{\Omega_{flat}} (\nabla_{x,y} g_i(r,\theta))^T (\nabla_{x,y} g_j(r,\theta))\, dxdy \\
&\qquad = \int_{\Omega_{flat}} (M\nabla_{r,\theta} g_i)^T (M\nabla_{r,\theta} g_j)\, rdrd\theta \\
&\qquad = \int_{\Omega_{flat}} (\nabla_{r,\theta} g_i)^T M^T M (\nabla_{r,\theta} g_j)\, rdrd\theta \\
&\qquad = \int_{\Omega_{flat}} \left(\frac{\partial g_i}{\partial r}, \frac{\partial g_i}{\partial \theta}\right) \begin{pmatrix} 1 & 0 \\ 0 & \frac{1}{r^2} \end{pmatrix} \begin{pmatrix} \frac{\partial g_j}{\partial r} \\ \frac{\partial g_j}{\partial \theta} \end{pmatrix} rdrd\theta \\
&\qquad = \int_{\Omega_{flat}} \left(\frac{\partial g_i}{\partial r}\frac{\partial g_j}{\partial r}\right) + \frac{1}{r^2}\left(\frac{\partial g_i}{\partial \theta}\frac{\partial g_j}{\partial \theta}\right)\, rdrd\theta. \qquad (36)
\end{aligned}$$

Since $g_k(r,\theta) = r^{(\frac{1}{2}+k)} \cos\left(\left(\frac{1}{2}+k\right)\theta\right)$,

$$\begin{aligned}
\frac{\partial g_i}{\partial r} &= \left(\frac{1}{2}+i\right) r^{i-\frac{1}{2}} \cos\left(\frac{1}{2}+i\right)\theta, \frac{\partial g_j}{\partial r} = \left(\frac{1}{2}+j\right) r^{j-\frac{1}{2}} \cos\left(\frac{1}{2}+j\right)\theta \quad (37) \\
\frac{\partial g_i}{\partial \theta} &= -\left(\frac{1}{2}+i\right) r^{\frac{1}{2}+i} \sin\left(\frac{1}{2}+i\right)\theta, \frac{\partial g_j}{\partial \theta} = -\left(\frac{1}{2}+j\right) r^{\frac{1}{2}+j} \sin\left(\frac{1}{2}+j\right)\theta. \quad (38)
\end{aligned}$$

Plugging (37) and (38) into (36), we have the following.

$$\begin{aligned}
&\int_{\Omega_{flat}} (\nabla_{x,y} g_i(r,\theta))^T (\nabla_{x,y} g_j(r,\theta))\, dxdy \\
&= \int_{\Omega_{flat}} \left(\frac{1}{2}+i\right)\left(\frac{1}{2}+j\right) r^{i+j} \cos\left(\left(\frac{1}{2}+i\right)\theta\right) \cos\left(\left(\frac{1}{2}+j\right)\theta\right) drd\theta \\
&\qquad + \int_{\Omega_{flat}} \left(\frac{1}{2}+i\right)\left(\frac{1}{2}+j\right) r^{i+j} \sin\left(\left(\frac{1}{2}+i\right)\theta\right) \sin\left(\left(\frac{1}{2}+j\right)\theta\right) drd\theta \\
&= \left(\frac{1}{2}+i\right)\left(\frac{1}{2}+j\right) \int_{\Omega_{flat}} r^{i+j} \left(\cos\left(\left(\frac{1}{2}+i\right)\theta - \left(\frac{1}{2}+j\right)\theta\right)\right) drd\theta \\
&= \left(\frac{1}{2}+i\right)\left(\frac{1}{2}+j\right) \int_{\Omega_{flat}} r^{i+j} \cos\left((i-j)\,\theta\right)\, drd\theta. \qquad (39)
\end{aligned}$$

which proves the theorem. □

Let I, J be the global indices corresponding to the local enrichment functions g_i, g_j,

respectively, and S_{IJ} be the $(I,J)^{th}$ component of stiffness matrix S. Then S_{IJ} is given by the following integration.

$$S_{IJ} = \int\limits_{O_i \cap O_j} (\nabla_{x,y}\Psi_i(x,y)g_i(r,\theta))^T(\nabla_{x,y}\Psi_j(x,y)g_j(r,\theta))\, dxdy, \tag{40}$$

where O_i and O_j are the supports of the partition of unity functions Ψ_i and Ψ_j, respectively. Recall that the functions g_i and g_j are globally defined functions. Then, the overlapping region $O_i \cap O_j$ can be decomposed as $O_{flat} \dot{\cup} O_{nonflat}$: a disjoint union of O_{flat} and $O_{nonflat}$. Since $\nabla\Psi_i = \nabla\Psi_j = (0,0)^T$ on O_{flat}, S_{IJ} of (40) can be written;

$$\begin{aligned} S_{IJ} &= \int\limits_{O_{flat}} (\nabla_{x,y}\Psi_i g_i)^T(\nabla_{x,y}\Psi_j g_j)\, dxdy + \int\limits_{O_{nonflat}} (\nabla_{x,y}\Psi_i g_i)^T(\nabla_{x,y}\Psi_j g_j)\, dxdy \\ &= \underbrace{\int\limits_{O_{flat}} (\nabla_{x,y} g_i)^T(\nabla_{x,y} g_j)\, dxdy}_{(A)} + \underbrace{\int\limits_{O_{nonflat}} (\nabla_{x,y}\Psi_i g_i)^T(\nabla_{x,y}\Psi_j g_j)\, dxdy}_{(B)}, \end{aligned}$$

where $\Psi_i = \Psi_i(x,y), \Psi_j = \Psi_j(x,y)$ and $g_i = g_i(r,\theta), g_j = g_j(r,\theta)$.

Let us examine (B) first. Note that Ψ_j is a piecewise polynomial and the integral region $O_{nonflat}$ is far away from the singularity of g_j. Also it is important to note that the integral region has a rectangular shape. Therefore, the integral (B) is straight forward to evaluate. With enough Gauss points, the integral (B) should be nearly exact.

Let $P : (r,\theta) \to (x,y)$ be the coordinate transformation:

$$x = r\cos\theta, y = r\sin\theta$$

and $T_R : (s,t) \to (x,y)$ be the patch mapping from the reference patch $\mathbf{P}$ to a quadrangle patch $\mathbf{R}$ (Figure 9). Then we have,

$$\begin{aligned}\frac{\partial}{\partial x}\left(\Psi_i g_i\right) &= \left(\frac{\partial \Psi_i}{\partial x}\right) g_i + \Psi_i \left(\frac{\partial g_i}{\partial r}\frac{\partial r}{\partial x} + \frac{\partial g_i}{\partial \theta}\frac{\partial \theta}{\partial x}\right) \\ &= \left(\frac{\partial \Psi_i}{\partial x}\right) g_i \circ P^{-1} + \Psi_i \left(\frac{\partial g_i}{\partial r}\cos\theta - \frac{\partial g_i}{\partial \theta}\frac{1}{r}\sin\theta\right) \circ P^{-1}. \qquad (41)\end{aligned}$$

Similarly,

$$\frac{\partial}{\partial x}\left(\Psi_j g_j\right) = \left(\frac{\partial \Psi_j}{\partial x}\right) g_j \circ P^{-1} + \Psi_j \left(\frac{\partial g_j}{\partial r}\cos\theta - \frac{\partial g_j}{\partial \theta}\frac{1}{r}\sin\theta\right) \circ P^{-1}, \qquad (42)$$

$$\frac{\partial}{\partial y}\left(\Psi_i g_i\right) = \left(\frac{\partial \Psi_i}{\partial y}\right) g_i \circ P^{-1} + \Psi_i \left(\frac{\partial g_i}{\partial r}\sin\theta + \frac{\partial g_i}{\partial \theta}\frac{1}{r}\cos\theta\right) \circ P^{-1}, \qquad (43)$$

$$\frac{\partial}{\partial y}\left(\Psi_j g_j\right) = \left(\frac{\partial \Psi_j}{\partial y}\right) g_j \circ P^{-1} + \Psi_j \left(\frac{\partial g_j}{\partial r}\sin\theta + \frac{\partial g_j}{\partial \theta}\frac{1}{r}\cos\theta\right) \circ P^{-1}. \qquad (44)$$

Note $\frac{\partial}{\partial x}\left(\Psi_j g_j\right)$, $\frac{\partial}{\partial x}\left(\Psi_j g_j\right)$, $\frac{\partial}{\partial y}\left(\Psi_i g_i\right)$, and $\frac{\partial}{\partial y}\left(\Psi_j g_j\right)$ are all function of x, y. Let us define $G(x,y) = \frac{\partial}{\partial x}\left(\Psi_i g_i\right)\frac{\partial}{\partial x}\left(\Psi_j g_j\right) + \frac{\partial}{\partial y}\left(\Psi_i g_i\right)\frac{\partial}{\partial y}\left(\Psi_j g_j\right)$. Then,

$$\begin{aligned}(B) &= \int\limits_{O_{nonflat}} \frac{\partial}{\partial x}\left(\Psi_i g_i\right)\frac{\partial}{\partial x}\left(\Psi_j g_j\right) + \frac{\partial}{\partial y}\left(\Psi_i g_i\right)\frac{\partial}{\partial y}\left(\Psi_j g_j\right) dxdy \\ &= \int\limits_{O_{nonflat}} G(x,y)dxdy = \int\limits_{P} G \circ T_R |J(T_R)| dsdt \\ &= \sum_{n=1}^{N_g}\sum_{m=1}^{N_g} G \circ T_B^k(g_n, g_m)|J(T_B^R)(g_n, g_m)|W_n W_m,\end{aligned}$$

where N_g is the number of Legendre-Gauss quadrature points, g_n is the Legendre-Gauss point, and W_n is the n-th quadrature weight.

On the other hand, by Theorem 4, Part (A) is as follows:

$$(A) = \left(\frac{1}{2}+i\right)\left(\frac{1}{2}+j\right)\int_{O_{flat}} r^{i+j}\cos\left(\left(i-j\right)\theta\right)\, drd\theta.$$

O_{flat} of the enriched patch can be further decomposed into two separate regions D and D^c. $D = \{(r,\theta)|0 \le r \le R, 0 \le \theta \le \pi\}$ in Figure 8 is the half disk and D^c is its

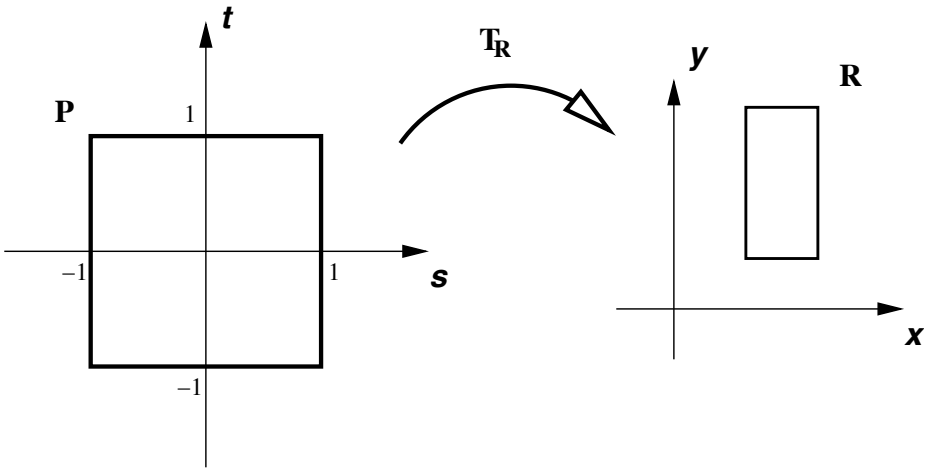

FIGURE 9: Rectangular Mapping T_R.

complement. i.e. $O_{flat} = D\dot{\cup}D^c$ (See Figure 8). On D, the integral of part (A) can be obtained exactly.

Then, the integral (A) over D can be simplified as follows:

$$\begin{cases} \left(\frac{1}{2}+i\right)\frac{\pi R^{2i+1}}{2} & \text{if } i=j, \\ 0 & \text{if } i\neq j. \end{cases} \tag{45}$$

Using (45), we have

$$(A) \;=\; \left(\frac{1}{2}+i\right)\frac{\pi R^{2i+1}}{2}\delta^i_j + \left(\frac{1}{2}+i\right)\left(\frac{1}{2}+j\right)\underbrace{\int_{D^c} r^{i+j}\cos\left((i-j)\,\theta\right)\,drd\theta}_{(C)},$$

where δ^i_j is the Kronecker delta. Now over the D^c region, we need to perform numerical integration because of its irregular shape. Since the D^c region is arch-shaped, we need to use the patch mapping of the blending type for this integration.

Remark *Note the integrand* $\cos\left((i-j)\,\theta\right)$ *becomes highly oscillatory as the value of* $|i-j|$ *increase. For instance, for* $i=40, j=1$ *the integrand oscillates about 20 times when the angle moves from 0 to* π*. Therefore, we need to divide the integral domain in the* θ*-direction. In an actual computation, the* θ*-direction integral was subdivided into 32 integrals to achieve a reasonable numerical accuracy.*

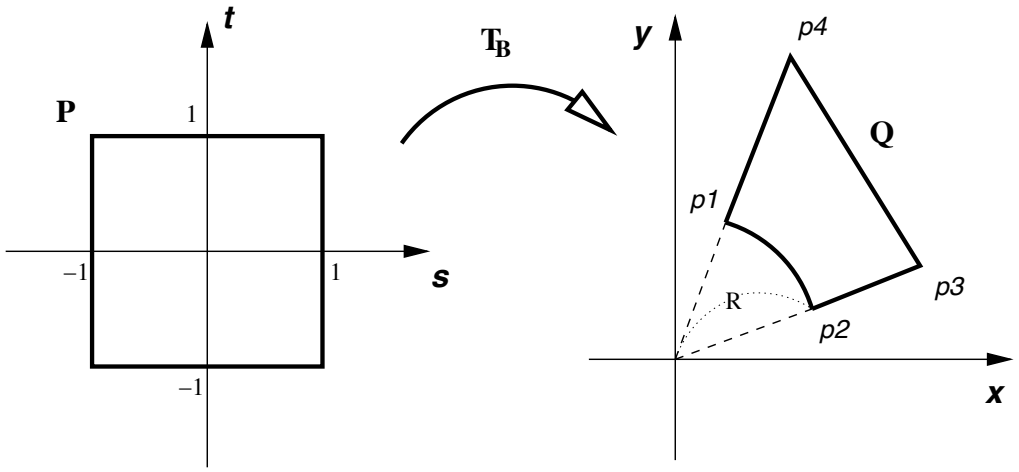

FIGURE 10: Blending Mapping T_B.

The blending mapping $T_B : (s,t) \to (x,y)$, Figure 10, maps the reference patch $\mathbf{P}$ onto a quadrangle $\mathbf{Q}$ with a curved side. Let $P1 = (R, \theta_2)$, $P2 = (R, \theta_1)$ in terms of polar coordinates and $P3 = (x_3, y_3)$, $P4 = (x_4, y_4)$ in rectangular coordinates. The blending patch mapping T_B is defined as follows:

$$\begin{cases} x &= \dfrac{1-t}{2}\left(R\cos\left(\dfrac{\theta_1-\theta_2}{2}\right)(s+1)+\theta_2\right)+\dfrac{1+t}{2}\left(x_3\left(\dfrac{1+s}{2}\right)+x_4\left(\dfrac{1-s}{2}\right)\right), \\ \\ y &= \dfrac{1-t}{2}\left(R\sin\left(\dfrac{\theta_1-\theta_2}{2}\right)(s+1)+\theta_2\right)+\dfrac{1+t}{2}\left(y_3\left(\dfrac{1+s}{2}\right)+y_4\left(\dfrac{1-s}{2}\right)\right). \end{cases}$$

Also its partial derivatives are as follows.

$$\frac{\partial x}{\partial s} = \frac{t-1}{2}\left(R\sin\left(\frac{\theta_1-\theta_2}{2}\right)(s+1)+\theta_2\right)\left(\frac{\theta_1-\theta_2}{2}\right)+\frac{1+t}{4}(x_3-x_4),$$

$$\frac{\partial x}{\partial t} = -\frac{1}{2}\left(R\cos\left(\frac{\theta_1-\theta_2}{2}\right)(s+1)+\theta_2\right)+\frac{1}{2}\left(x_3\left(\frac{1+s}{2}\right)+x_4\left(\frac{1-s}{2}\right)\right),$$

$$\frac{\partial y}{\partial s} = \frac{1-t}{2}\left(R\cos\left(\frac{\theta_1-\theta_2}{2}\right)(s+1)+\theta_2\right)\left(\frac{\theta_1-\theta_2}{2}\right)+\frac{1+t}{4}(y_3-y_4),$$

$$\frac{\partial y}{\partial t} = -\frac{1}{2}\left(R\sin\left(\frac{\theta_1-\theta_2}{2}\right)(s+1)+\theta_2\right)+\frac{1}{2}\left(y_3\left(\frac{1+s}{2}\right)+y_4\left(\frac{1-s}{2}\right)\right).$$

The determinant of Jacobian (T_B), denoted by $|J(T_B)|$, is $\dfrac{\partial x}{\partial s}\dfrac{\partial y}{\partial t} - \dfrac{\partial x}{\partial t}\dfrac{\partial y}{\partial s}$. Hence integral over region Q can be transformed over region P.

$$\int_Q F(x,y)dxdy = \int_P F \circ T_B \left(\frac{\partial x}{\partial s}\frac{\partial y}{\partial t} - \frac{\partial x}{\partial t}\frac{\partial y}{\partial s} \right) dsdt.$$

As pointed out earlier to obtain accurate numerical integration, the D^c region should be partitioned into many pieces to capture the oscillatory behavior of the integrand. Let us say D^c is partitioned into N pieces. Also let T_B^k be the transformation from the reference square P into the integral region D_k^c, where $D^c = \bigcup_{k=1}^N D_k^c$. Then the integral (C) becomes the following.

$$\begin{aligned}
(C) &= \sum_{k=1}^{N} \int_{D_k^c} r^{i+j} \cos\left((i-j)\,\theta\right) drd\theta \\
&= \sum_{k=1}^{N} \int_{P} \left(r^{i+j} \cos\left((i-j)\,\theta\right) \right) \circ T_B^k |J(T_B^k)| dsdt \\
&= \sum_{k=1}^{N} \int_{-1}^{1} \int_{-1}^{1} \left(r^{i+j} \cos\left((i-j)\,\theta\right) \right) \circ T_B^k |J(T_B^k)| dsdt \\
&= \sum_{k=1}^{N} \sum_{n=1}^{N_g} \sum_{m=1}^{N_g} \left(r^{i+j} \cos\left((i-j)\,\theta\right) \right) \circ T_B^k(g_n, g_m) |J(T_B^k)(g_n, g_m)| W_n W_m
\end{aligned}$$

where N_g denotes the number of Legendre-Gauss quadrature points, g_n denotes the Legendre-Gauss point, W_n is the n-th quadrature weight. Thus, we have completed the calculation of S_{IJ}.

On the other hand, since the Motz problem is a Laplace equation, calculating the load vector is straightforward. Using the Kronecker delta property of the basis functions, imposing essential boundary condition is as simple as in the conventional finite element method. Therefore, unlike other meshless methods, our GFEM solution of the Motz problem does not have any error related to the Dirichlet boundary conditions because the essential boundary conditions are constants, and local approximation functions have the polynomial reproducing property.

2.3 Numerical Results

The numerical tests are carried out by using the RPP shape functions of polynomial reproducing orders 2,4,6, and 8 on each of the 38 rectangular patches that do not contain the singularity and 40 enriched singular functions on the enrichment patch containing the singularity. Figure 11 and Figure 12 shows that the singular behavior of the Motz problem was removed by the use of 40 enriched approximation functions. On the enrichment patch, one can see that for order 6 and 8 there is virtually no error because of using the enriched basis functions in Figure 12. It is worthwhile to note that the degrees of freedom to capture the singularity at the enrichment patch is only 40. Also the condition number for each case is comparably small and does not grow quickly due to the wide flat-top of the partition of unity function.

Table 1 contains the numerical results obtained by GFEM with the use of enriched approximation functions for the Motz problem. It is known that the numerical solution of the Motz problem obtained by Li et al. (1987) is the most accurate one. In Table 1, the errors in the max norm as well as the energy norm are computed using the best known solution (Li et al., 1987) as the true solution. The maximum errors of our method are depicted in Figures 11 and 12.

The strain energy of $u \in H^1(\Omega)$, is $\mathcal{U} = \frac{1}{2}\mathcal{B}(u,u)$. The error in the energy norm is defined by

$$\left| \frac{\mathcal{U}^{\text{gfem}} - \mathcal{U}^{\text{Li}}}{\mathcal{U}^{\text{Li}}} \right|^{\frac{1}{2}},$$

where $\mathcal{U}^{\text{gfem}}$ is the strain energy obtained by the method that is used in this dissertation and $\mathcal{U}^{Li}$ is the energy that is obtained by the solution provided in the literature (Li et al., 1987).

When the structure of the singularity is known, RSPM(Reproducing Singularity Particle Methods) is more effective than the adaptive RPPM(Oh and Jeong, 2009). RSPM is a Galerkin approximation method associated with the use of RSP shape

TABLE 1: GFEM with enriched basis function results.

rpp order	**dof**	$\|\mathbf{err}\|_{max}$	$\|\mathbf{err}\|_{energy}$
2	349	2.75×10^{-3}	7.24×10^{-5}
4	940	5.69×10^{-7}	1.87×10^{-6}
6	1830	2.13×10^{-8}	1.74×10^{-7}
8	3019	5.37×10^{-9}	4.37×10^{-8}

functions on the patches containing singularities and with the use of RPP shape functions on other patches for local approximation functions. Thus, RSPM is similar to the Method of Auxiliary Mapping (Lucas and Oh, 1993, Oh and Babuska, 1995, Oh et al., 1998, 2001) in the framework of the p-version FEM. Table 2 compares the best performance of enriched GFEM, RSPM, and p-FEM with MAM. We conclude GFEM with basis enrichment is superior to both RSPM and p-FEM with MAM for the Motz problem. Therefore, when the nature of the singularity is known, GFEM with enrichment is preferred. Also it is important to note that both p-version FEM with MAM and RSPM can not estimate d_i in (34) but enriched GFEM can.

TABLE 2: Relative energy norm error comparison with other methods.

p degree	**p-FEM with MAM**	**Meshless RSPM**	**GFEM with enrichment**
2	9.00×10^{-3}	1.54×10^{-2}	7.24×10^{-5}
4	2.38×10^{-4}	3.17×10^{-4}	1.87×10^{-6}
6	3.42×10^{-6}	2.40×10^{-5}	1.74×10^{-7}
8	4.83×10^{-8}	7.23×10^{-7}	4.37×10^{-8}

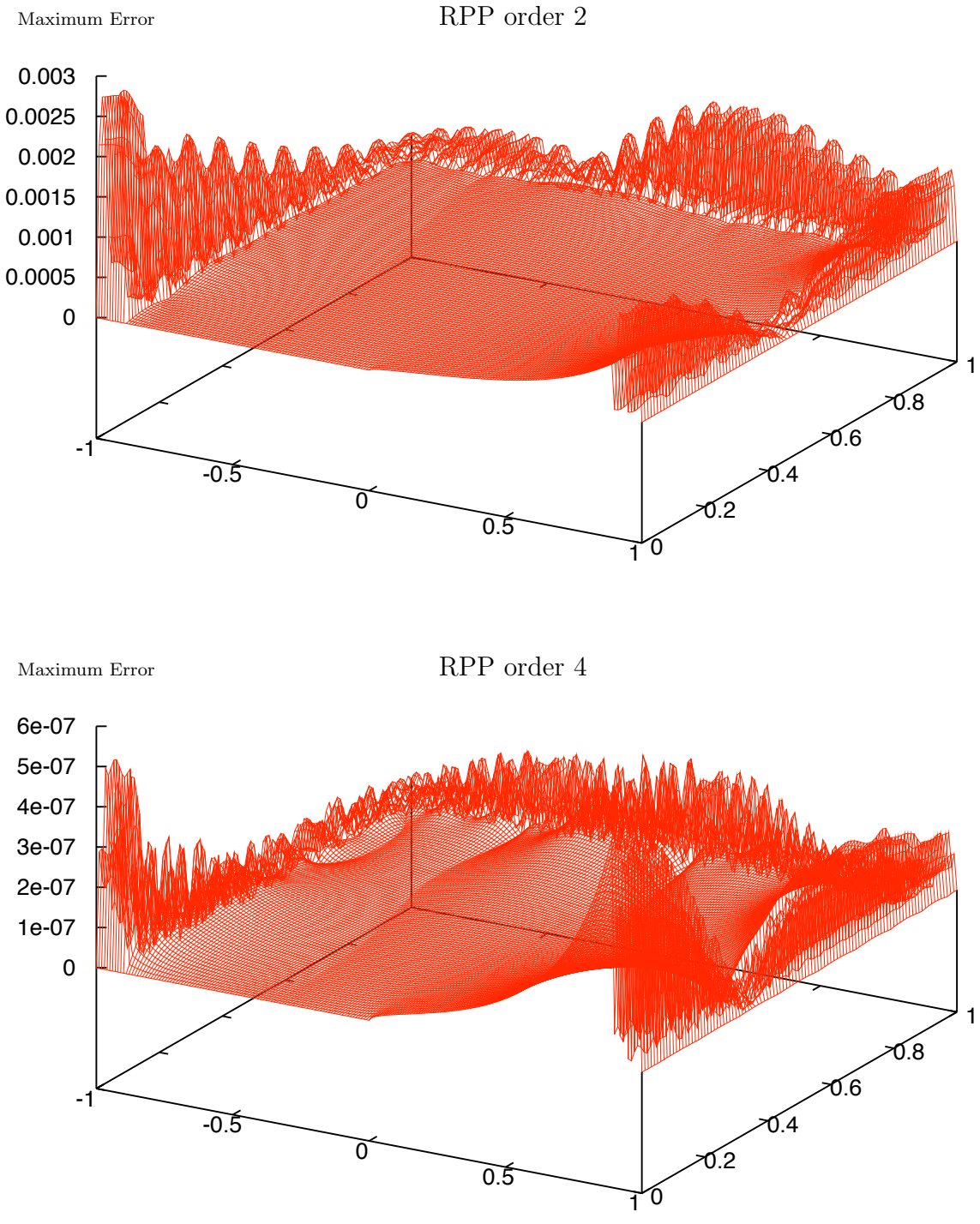

FIGURE 11: RPP order 2 and 4 with 40 Enriched Basis.

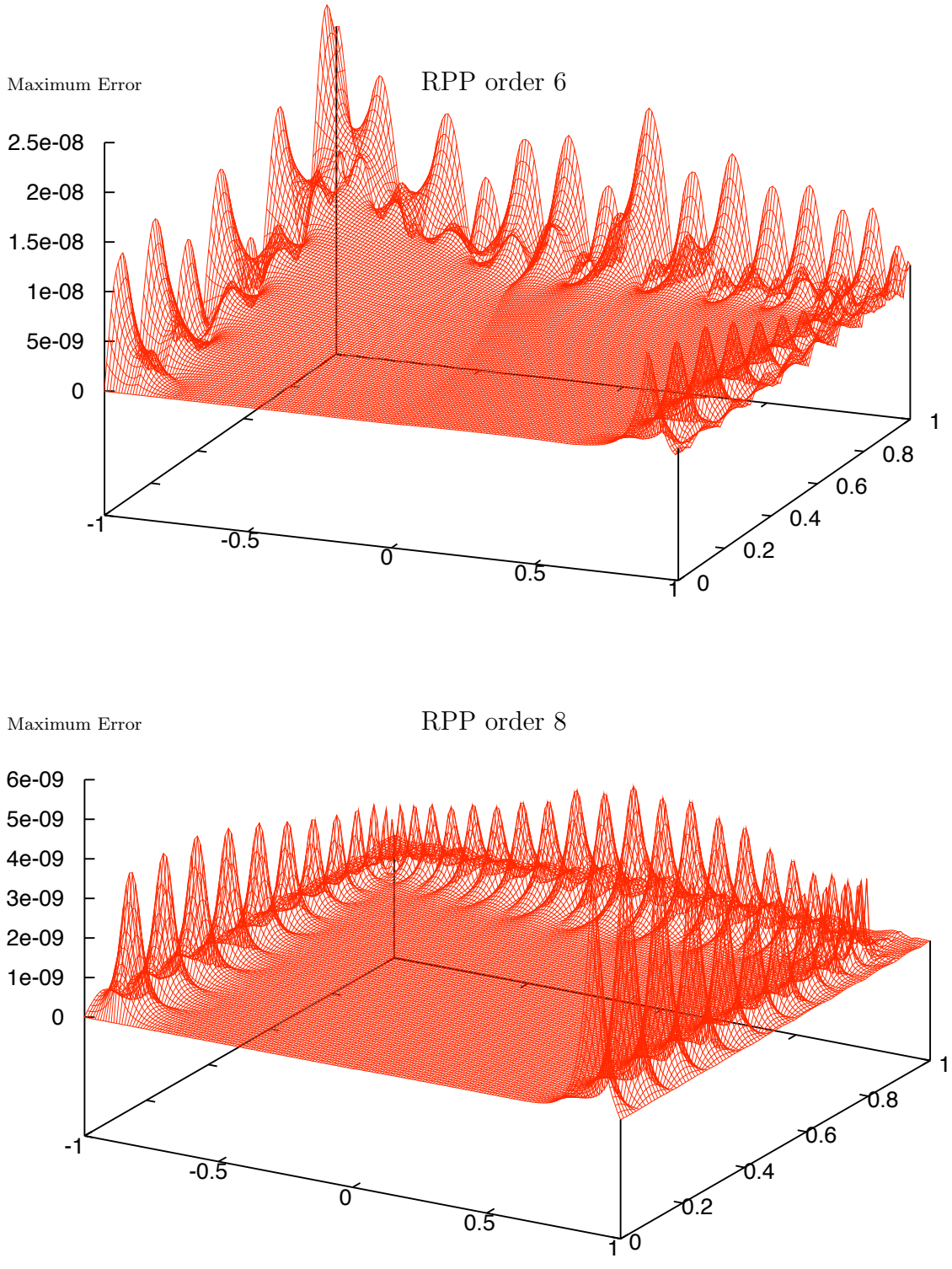

FIGURE 12: RPP order 6 and 8 with 40 Enriched Basis.

Let us note that our enriched GFEM solution has no errors along Γ_2 because the local approximation functions on the patches along Γ_2 have the Kronecker delta property and exactly interpolate polynomials (the reproducing polynomial property). Hence, in terms of boundary condition imposition enriched GFEM solution is clearly better than Li et al. (1987)'s solution. Figure 12 shows the maximum difference between enriched GFEM solution and Li et al. (1987)'s solution is less than 6×10^{-9}.

To compare the accuracy of $\tilde{d}_i$ in our approximate solution (35) with that of Li et al. (1987), we compare the errors of $\sum_{i=0}^{39} \tilde{d}_i^{\text{gfem}} r^{i+\frac{1}{2}} \cos(i+\frac{1}{2})\theta$ and $\sum_{i=0}^{34} \tilde{d}_i^{\text{Li}} r^{i+\frac{1}{2}} \cos(i+\frac{1}{2})\theta$ along the boundary Γ_2 where the true solution is 500. Result is given in the Figure 13. Here $\tilde{d}_i^{\text{gfem}}, i = 0, \cdots, 39$ is the coefficient that was obtained by the GFEM with enrichment, and $\tilde{d}_i^{\text{Li}}, i = 0, \cdots, 34$ is the coefficient that is listed in Li et al. (1987). Note $\sum_{i=0}^{39} \tilde{d}_i^{\text{gfem}} r^{i+\frac{1}{2}} \cos(i+\frac{1}{2})\theta$ is not GFEM solution itself but $\tilde{d}_i^{\text{gfem}}, i = 0, \cdots, 39$ can be obtained because we used $r^{i+\frac{1}{2}} \cos(i+\frac{1}{2})\theta, i = 0, \cdots, 39$ as enriched basis functions. i.e. having 40 singular basis functions on the enriched patch, it is possible to obtain accurate coefficients $\tilde{d}_i$ in the partial sum (35). The $\tilde{d}_i$ can be directly obtained from the finite element solution (23). The Table 3 shows the coefficients $\tilde{d}_i$, $i = 1, \cdots, 40$.

Remark *Those existing numerical methods, Table 4, such as Boundary Methods (Li et al., 1987), Collocation Trefftz Methods (Lu et al., 2004), Integrated Singular Basis Function Methods (Georgiou et al., 1996), needs special treatment to accurately impose boundary conditions. However, imposing the essential boundary conditions in our method is straight forward because our basis functions near* Γ_2 *not only satisfy the Kronecker delta property but also reproduce polynomial.*

The numerical methods, proposed for the Motz problem, include the finite difference, the global element, the boundary element, and the finite element. The best numerical solution for the Motz problem that is known so far (Li et al., 1987) has maximum absolute error 5.47×10^{-9} on Γ_2. In this dissertation, using GFEM with

use of enriched basis functions, the absolute maximum error reaches 6.89×10^{-9} on Γ_2. The two solutions have almost the same accuracy along Γ_2. Let us note that Li's solution has 35 coefficients, and the numerical solution by the proposed method has 40 coefficients.

However, we claim that GFEM with the use of enriched basis functions can effectively handle not only monotone singularities (of type r^α with $\alpha < 1$) but oscillating singularities (of the type $r^\alpha \sin(\epsilon \log r)$) (Oh et al., 2001). On the other hand, the method used in (Li et al., 1987) is not effective in handling oscillating singularities.

FIGURE 13: Comparison between the best known solution on Γ_2.

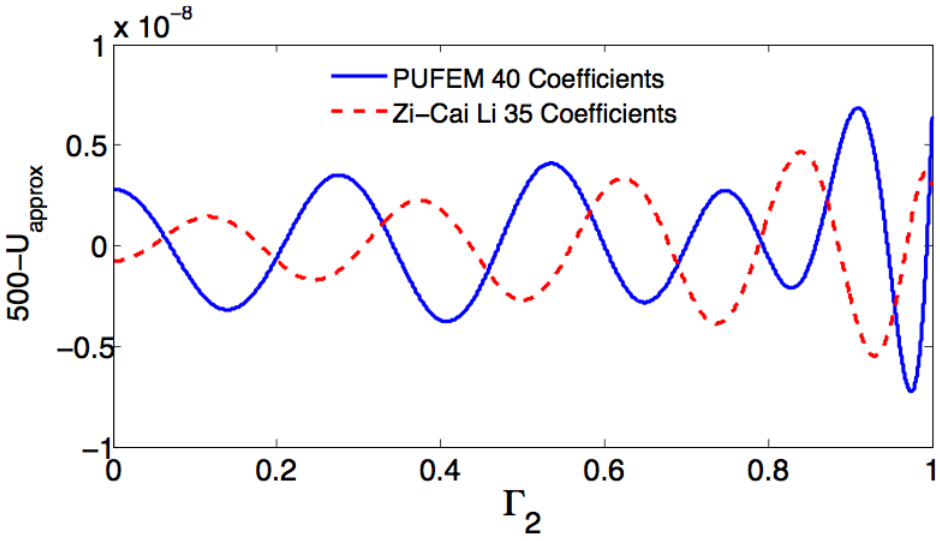

Since our local approximation functions have the Kronecker delta property and the polynomial reproducing property, it is possible to impose essential boundary conditions exactly along Γ_2. Figure 12 shows that the GFEM solution has no error along Γ_2, even though the partial sum $\sum_{i=0}^{39} \tilde{d}_i r^{i+\frac{1}{2}} \cos(i+\frac{1}{2})\theta$ can not be 500 along Γ_2.

Remark *In the maximum norm, Li's solution is slightly better than our solution: That is,* $||error||_{\Gamma_2,\infty} = 5.47 \times 10^{-9}$ *(Li et al.) and* $||error||_{\Gamma_2,\infty} = 6.89 \times 10^{-9}$

(Our method). Moreover, if we compare those errors in the mean square norm along Γ_2*, the accuracy of our solution is closer to that of Li's solution : That is,* $||error||_{\Gamma_2,L_2} = 2.26 \times 10^{-9}$ *(Li et al.) and* $||error||_{\Gamma_2,L_2} = 2.78 \times 10^{-9}$*. Although the accuracy of Li's solution on* Γ_2 *is slightly better, the GFEM method with 40 enrichment functions has more significant digits for leading coefficients* $\tilde{d}_i$ *(See Table 4).*

In order to show the effectiveness of the GFEM with enrichment, the first 25 coefficients $\tilde{d}_j$ of the partial sum (35) obtained by various numerical methods are compared in Table 4. We conclude that the proposed method results in highly accurate coefficients $\tilde{d}_i$, for the first several terms. Especially, the first coefficient has at least 13 significant digits.

Later in Chapter 3, we will estimate the stress intensity factor using GFEM with enrichment. Linear elasticity is nothing but coupled elliptic equations. Hence, the described method should work well for the elasticity problem. The highly accurate leading coefficient enables us to compute the stress intensity factor in a non-conventional way.

TABLE 3: Computed coefficients $\tilde{d}_i$ of $\sum_{i=1}^{40} \tilde{d}_i r^{i+\frac{1}{2}} \cos((i+\frac{1}{2})\theta)$.

ith		**Coefficients**	**ith**		**Coefficients**
1	+	401.1624537452345	21	+	2.290744823584897e-06
2	+	87.65592019508790	22	+	1.063692985558411e-06
3	+	17.23791507944674	23	+	5.314980562968453e-07
4	−	8.071215259682478	24	−	2.454035587720472e-07
5	+	1.440272717022879	25	+	1.094258200815170e-07
6	+	3.310548859207677e-01	26	+	5.204123234110838e-08
7	+	2.754373445087275e-01	27	+	2.594548101382485e-08
8	−	8.693299465893235e-02	28	−	1.091753910227160e-08
9	+	3.360487861931393e-02	29	+	5.274360833540486e-09
10	+	1.538437428404088e-02	30	+	2.733609395521398e-09
11	+	7.302301728215649e-03	31	+	1.354076917219339e-09
12	−	3.184113774923665e-03	32	−	1.816851682230465e-10
13	+	1.220646385725587e-03	33	+	2.266480380995557e-10
14	+	5.309652968145126e-04	34	+	1.541467769079195e-10
15	+	2.715121558566150e-04	35	+	7.396367522015557e-11
16	−	1.200455757406748e-04	36	+	5.058240306963314e-11
17	+	5.053973008462738e-05	37	+	6.165507191581204e-12
18	+	2.316701639900009e-05	38	+	6.544346229722119e-12
19	+	1.153538904754159e-05	39	+	2.943942531164191e-12
20	−	5.293975100353315e-06	40	+	5.127853852958069e-12

TABLE 4: Comparison of the calculated coefficients to other methods.

i	Exact N=20 (1975)	Li et al. N=35 (1987)	ISBFM N=40 (1991)	SFBIM N=75 (1996)	TREFFTZ N=35 (2004)	GFEM N=40 Present
1	401.1624537452	401.1624537450	401.1624537452	401.1624537452	401.1624537452344	401.1624537452345
2	87.6559201951	87.6559201941	87.6559202595	87.6559201951	87.6559201950879 3	87.6559201950879 0
3	17.2379150794	17.2379150819	17.2379150363	17.2379150794	17.2379150794467 8	17.2379150794467 4
4	-8.0712152597	-8.0712152607	-8.0712152597	-8.0712152597	-8.0712152596 98	-8.0712152596 82
5	1.4402727170	1.4402727163	1.4402727171	1.4402727170	1.4402727170 22	1.4402727170 22
6	0.3310548859	0.3310548866	0.3310548859	0.3310548859	0.3310548859 2	0.3310548859 2
7	0.2754373445	0.2754373447	0.2754373443	0.2754373445	0.2754373445 0	0.2754373445 0
8	-0.0869329945	-0.0869329948	-0.0869329946	-0.0869329945	-0.0869329945 0	-0.0869329946 5
9	0.0336048784	0.0336048781	-0.0336048784	0.0336048784	0.0336048784 0	0.0336048786 1
10	0.0153843745	0.0153843747	0.0153843745	0.0153843745	0.0153843744 45	0.0153843742 84
11	0.0073023017	0.0073023019	0.0073023017	0.0073023017	0.0073023016 4	0.0073023017 2
12	-0.0031841139	-0.0031841138	-0.0031841139	-0.0031841139	-0.0031841136 1	-0.0031841137 7
13	0.0012206461	0.0012206456	0.0012206461	0.0012206461	0.0012206458 6	0.0012206463 8
14	0.0005309655	0.0005309655	0.0005309655	0.0005309655	0.0005309652 9	0.0005309652 9
15	0.0002715122	0.0002715122	0.0002715122	0.0002715122	0.0002715120 2	0.0002715121 5
16	-0.0001200463	-0.0001200450	-0.0001200464	-0.0001200464	-0.0001200450 4	-0.0001200455 7
17	0.0000505400	0.0000505387	0.0000505398	0.0000505398	0.0000505389 2	0.0000505397 3
18	0.0000231667	0.0000231664	0.0000231668	0.0000231669	0.0000231662 5	0.0000231670 1
19	0.0000111535	0.0000115349	0.0000115352	0.0000115353	0.0000115348 4	0.0000115353 8
20	-0.0000052951	-0.0000052931	-0.0000052957	-0.0000052958	-0.0000052932 3	-0.0000052939 7
21		0.0000022895	0.0000022911	0.0000022911	0.0000022897 5	0.0000022974 4
22		0.0000010624	0.0000010632	0.0000010635	0.0000010623 9	0.0000010636 9
23		0.0000005307	0.0000005312	0.0000005314	0.0000005307 2	0.0000005314 9
24		-0.0000002449	-0.0000002473	-0.0000002474	-0.0000002450 7	-0.0000002454 0
25		0.0000001085	0.0000001097	0.0000001087	0.0000001086 4	0.0000001094 2

CHAPTER 3: STRESS ANALYSIS ON CRACKED ELASTIC DOMAINS

3.1 The Elasticity Equations

Let Ω be an elastic medium in $\mathbb{R}^2$ with boundary $\Gamma = \partial\Omega$. The state variables (the displacement vectors) are denoted by $u = \{u^x(x,y), u^y(x,y)\}^T$ and stress tensor are denoted by $\{\sigma^{(u)}\} = \{\sigma_x^{(u)}, \sigma_y^{(u)}, \tau_{xy}^{(u)}\}^T$. Let us denote the strain tensor $\{\varepsilon^{(u)}\} = \{\varepsilon_x^{(u)}, \varepsilon_y^{(u)}, \gamma_{xy}^{(u)}\}$.

The strain-displacement and stress-strain relations are given by

$$\{\varepsilon^{(u)}\} = [D]\{u\}, \tag{46}$$

$$\{\sigma^{(u)}\} = [\mathbf{E}]\{\varepsilon^{(u)}\}, \tag{47}$$

respectively, where $[D]$ is the following differential matrix,

$$[D] = \begin{bmatrix} \frac{\partial}{\partial x} & 0 \\ 0 & \frac{\partial}{\partial y} \\ \frac{\partial}{\partial y} & \frac{\partial}{\partial x} \end{bmatrix}, \tag{48}$$

and $[\mathbf{E}] = [\mathbf{E}_{ij}], 1 \leq i,j \leq 3$, is a symmetric positive definite matrix of material constants.

For a isotropic elastic medium, the matrix $[\mathbf{E}]$ is given as :

$$[\mathbf{E}] = \frac{E}{1-\nu^2} \begin{bmatrix} 1 & \nu & 0 \\ \nu & 1 & 0 \\ 0 & 0 & \frac{1-\nu}{2} \end{bmatrix} \tag{49}$$

when plane stress is the quantity of interest, or

$$[\mathbf{E}] = \begin{bmatrix} \zeta + 2\mu & \zeta & 0 \\ \zeta & \zeta + 2\mu & 0 \\ 0 & 0 & \mu \end{bmatrix} \tag{50}$$

when plane strain is the quantity of interest. Here, μ and ζ are defined as follows:

$$\mu = \frac{E}{2(1+\nu)}, \quad \zeta = \frac{\nu E}{(1+\nu)(1-2\nu)}. \tag{51}$$

Note that E is the modulus of elasticity and ν ($0 \leq \nu < \frac{1}{2}$) is Poisson's ratio.

The equilibrium equations of elasticity are given by

$$[D]^T\{\sigma^{(u)}\}(x,y) + \{f\}(x,y) = 0, \quad (x,y) \in \Omega, \tag{52}$$

where $\{f\} = \{f_x(x,y), f_y(x,y)\}^T$ is the vector that describes body force per unit area.

Using the stress-strain relation, (46) and (47), (52) can be expressed in terms of the displacement vector $\{u\}$. Let us consider the following system of partial differential equations in terms of the displacement vector,

$$[D]^T[\mathbf{E}][D]\{u\}(x,y) + \{f\}(x,y) = 0, (x,y) \in \Omega, \tag{53}$$

subject to the following boundary conditions,

$$[N]\{\sigma^{(u)}\}(s) = \{\tilde{T}\}(s) = \{\tilde{T}_x(s), \tilde{T}_y(s)\}^T, s \in \Gamma_N, \tag{54}$$

$$\{u\}(s) = \{\tilde{u}\}(s) = \{\tilde{u}_x(s), \tilde{u}_y(s)\}^T, s \in \Gamma_D, \tag{55}$$

where $\Gamma = \Gamma_N \cup \Gamma_D = \partial\Omega$, $\{n_x, n_y\}^T$ is an outward unit normal vector to the traction boundary Γ_N, and

$$[N] = \begin{bmatrix} n_x & 0 & n_y \\ 0 & n_y & n_x \end{bmatrix}. \tag{56}$$

Let $\mathbf{H_D^1}(\Omega) = \{\{w\} = \{w_x, w_y\} \in [\mathbf{H^1}(\Omega)]^2 : \{w\} = 0 \text{ on } \Gamma_D\}$. Then the varia-

tional form of (53)-(55) become the following:

Find the vector $\{u\} = \{u^x, u^y\}$ such that $u^x, u^y \in H^1(\Omega)$, $\{u\} = \{\tilde{u}\}$ on Γ_D, and

$$\mathcal{B}(\{u\}, \{v\}) = \mathcal{F}(\{v\}) \text{ for all } \{v\} \in \mathbf{H_D^1}(\Omega), \tag{57}$$

where,

$$\mathcal{B}(\{u\}, \{v\}) = \int_\Omega ([D]\{v\})^T [E]([D]\{u\}) dxdy, \tag{58}$$

$$\mathcal{F}(\{v\}) = \int_\Omega \{v\}^T \{f\} dxdy + \oint_{\Gamma_N} \{v\}^T \{\tilde{T}\} ds. \tag{59}$$

$\mathcal{U}(\{u\}) = \frac{1}{2}\mathcal{B}(\{u\}, \{v\})$ is the strain energy of the displacement vector $\{u\}$.

Let us denote the basis functions defined on Ω by $\Phi_i(x, y), i = 1, 2, \cdots, n$. The components of the displacement vector in terms of basis functions Φ_i are given as the following forms:

$$u^x(x, y) = \sum_{k=1}^{n} c_k \Phi_k(x, y), \tag{60}$$

$$u^y(x, y) = \sum_{k=n+1}^{n} c_{n+k} \Phi_k(x, y), \tag{61}$$

where $c_i \quad (i = 1, 2, \cdots, 2n)$ are called the amplitudes of the basis functions Φ_i. Let

$$\{\Phi_k\} = \begin{pmatrix} \Phi_k(x, y) \\ 0 \end{pmatrix}, k = 1, 2, \cdots, n, \tag{62}$$

$$\{\Phi_k\} = \begin{pmatrix} 0 \\ \Phi_k(x, y) \end{pmatrix}, k = n+1, 2, \cdots, 2n. \tag{63}$$

Then the displacement vector $\{u\}$ can be written as

$$\{u\} = \sum_{k=1}^{2n} a_k \{\Phi_k\}.$$

Substituting (62) and (63) into (58), we have the following.

Lemma 3 *The bilinear form* $\mathcal{B}(\{u\},\{v\})$ *on an element* e *becomes,*

$$\int_e (\nabla\Phi_j)^T \begin{bmatrix} E_{11} & E_{13} \\ E_{31} & E_{33} \end{bmatrix} (\nabla\Phi_i) \text{ if } \{v\} = \{\Phi_i, 0\}^T \{u\} = \{\Phi_j, 0\}^T, \tag{64}$$

$$\int_e (\nabla\Phi_j)^T \begin{bmatrix} E_{33} & E_{32} \\ E_{23} & E_{22} \end{bmatrix} (\nabla\Phi_i) \text{ if } \{v\} = \{0, \Phi_i\}^T \{u\} = \{0, \Phi_j\}^T, \tag{65}$$

$$\int_e (\nabla\Phi_j)^T \begin{bmatrix} E_{13} & E_{12} \\ E_{33} & E_{32} \end{bmatrix} (\nabla\Phi_i) \text{ if } \{v\} = \{\Phi_i, 0\}^T \{u\} = \{0, \Phi_j\}^T, \tag{66}$$

$$\int_e (\nabla\Phi_j)^T \begin{bmatrix} E_{31} & E_{33} \\ E_{21} & E_{23} \end{bmatrix} (\nabla\Phi_i) \text{ if } \{v\} = \{0, \Phi_i\}^T \{u\} = \{\Phi_j, 0\}^T. \tag{67}$$

3.2 Partition of unity for edge-cracked domains

Constructing a partition of unity for a background mesh of a non-convex domain such as an edge-cracked domain was not obvious. For this purpose, recently Oh et al. (2009) introduced a new method called the *almost everywhere partition of unity*. Instead of using the almost everywhere partition of unity, we use a polar mapping to construct a partition of unity on edge-cracked domains.

To illustrate how to construct a partition of unity on a *non-convex* single edge-cracked domain, let us consider the background mesh in Figure 14 (a). We use eight patches $Q_J, J = \mathrm{I}, \mathrm{II}, \cdots, \mathrm{VIII}$ as shown in Figure 14 (a). For each patch Q_J, we construct a partition of unity function Ψ_J that corresponds to the patch Q_J. The support of the partition of unity function Ψ_J is illustrated by dotted lines in Figure 14 (b). For example, the support of Ψ_{III} is the shaded region in Figure 14 (c). The thin strips that are enclosed by dotted lines are the overlapping region of the partition of unity functions. Note that the supports of the partition of unity functions do not overlap along the negative x-axis where the crack line is located.

Let $P : (r, \theta) \rightarrow (x, y)$ be the coordinate transformation:

$$x = r\cos\theta, \quad y = r\sin\theta.$$

Then, as shown in the Figure 14, through the mapping P, the partition of unity on the cracked domain in the polar coordinate system (Figure 14 (c) left) is generated by using the partition of unity of the reference domain in the rectangular coordinate system (Figure 14 (c) right).

Let the partition of unity function on the reference coordinate system be $\hat{\Psi}_J(r, \theta)$ (J=I,II,$\cdots$,VIII). This reference partition of unity functions $\hat{\Psi}_J(r, \theta)$ can be easily constructed by using the tensor product of (9). Then the partition of unity functions $\Psi_J(x, y)$ on the physical coordinate system is given by,

$$\Psi_J(x, y) = \hat{\Psi}_J \circ P^{-1}(x, y), \quad J = \mathrm{I}, \mathrm{II}, \cdots, \mathrm{VIII}.$$

Note that P is not *one-to-one*. To define P^{-1}, we assume $P^{-1}(0, 0) = (0, 0)$. Then in this configuration, $\Psi_J(0, 0) = 1$, $J = 1, 2, \cdots, 8$. That is,

$$\sum_{J=1}^{8} \Psi_J(0, 0) = 8 \neq 1.$$

$\Psi_J(x, y)$ fails to be a partition of unity at one point. We call $\Psi_J(x, y)$, the *almost everywhere partition of unity* (Oh and Jeong, 2008).

Because of the mapping P, the gradient of the four partition of unity functions $\Psi_J(x, y)$ J=I,II,$\cdots$,IV become arbitrary large on the overlapping region when $\sqrt{x^2 + y^2} \rightarrow 0$. However, due to the nodal constraint, this fact does not cause any computational problems. For more general and detailed analysis, we refer to (Oh and Jeong, 2008).

As shown in Figure 14 (c), the four outer patches, $Q_J, J = \mathrm{I}, \mathrm{II}, \cdots, \mathrm{VIII}$ are mapped to quadrangles, $\hat{Q}_J, J = \mathrm{I}, \mathrm{II}, \cdots, \mathrm{VIII}$ with one curved side. All calculations are straight forward except the line integral on the curved boundary.

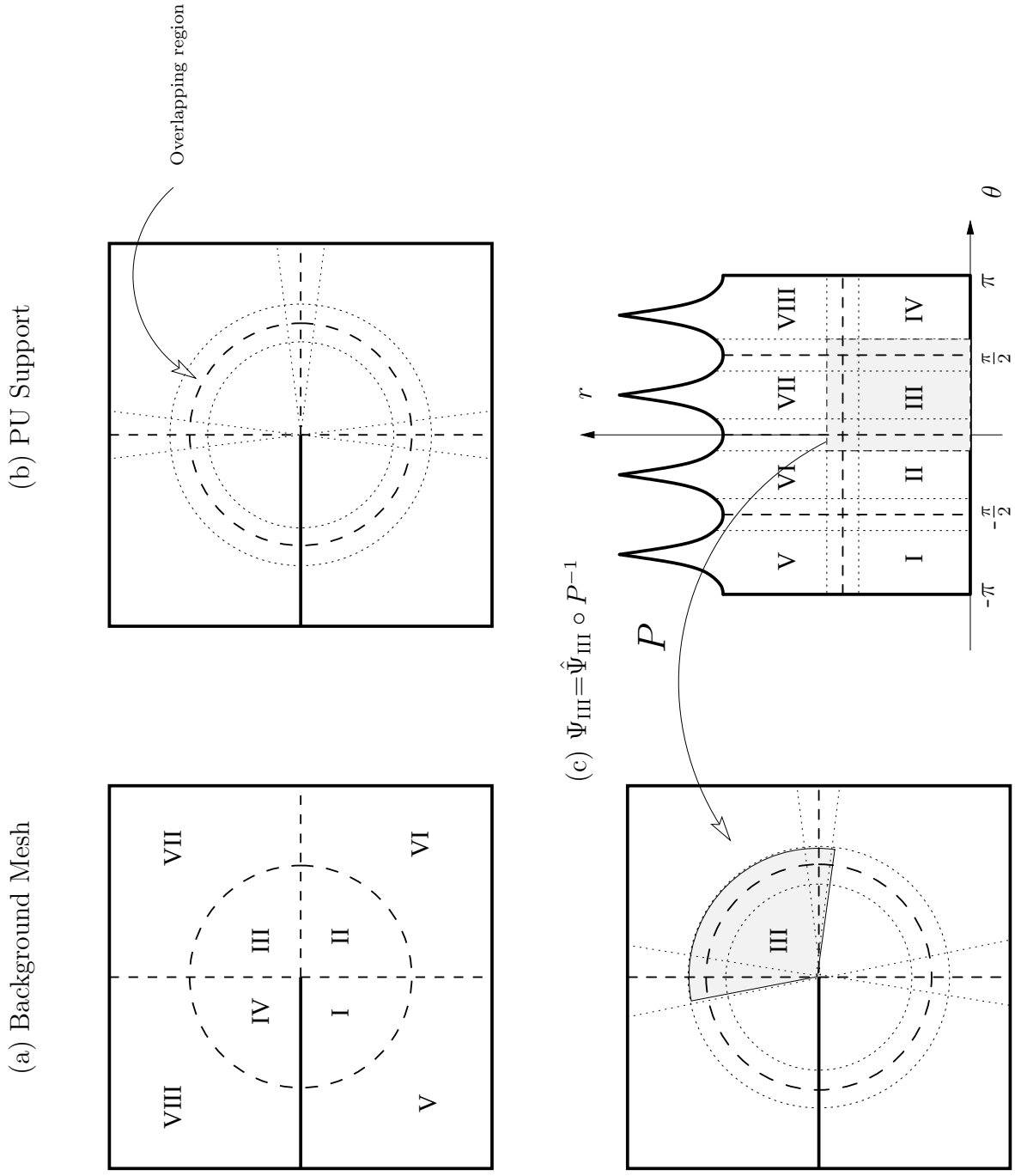

FIGURE 14: Partition of Unity for the Edge-Cracked Domain.

3.3 Elasticity problems containing singularities

For the numerical tests of GFEM with enriched basis functions, we choose the following approximation space V_h^{enrich}.

$$V_h^{\text{enrich}} = \text{span}\{b_{Jk}(x,y), s_{Ji}(x,y) : k = 1,..,N_J, i = 1,..,S_J, J = 1,..,M\} \tag{68}$$

where b_{Jk} and $s_{J,i}$ are as follows:

$$b_{Jk}(x,y) := \Psi_J(x,y) f_k(x,y), \quad s_{Ji}(x,y) := \Psi_J(x,y) g_i(x,y).$$

Remark *$S_J = 0$ if the patch Q_J is not enriched.*

Here $f_k(x,y)$ are RPP local approximation functions, $g_i(x,y)$ are singular enriched functions, and also $\Psi_J(x,y)$ is the PU function on the patch Q_J.

Then the Galerkin approximation,$\{u_h\} = \{u_h^x, u_h^y\}$, for each component of the vector $\{u\} = \{u^x, u^y\}$ is the following.

$$u_h^x(x,y) = \sum_{J=1}^{M}(\sum_{k=1}^{N_J} c_{Jk} b_{Jk} + \sum_{i=1}^{S_J} d_{Ji} s_{Ji}) \tag{69}$$

$$u_h^y(x,y) = \sum_{J=1}^{M}(\sum_{k=1}^{N_J} c_{J+1k} b_{Jk} + \sum_{i=1}^{S_J} d_{J+1i} s_{Ji}) \tag{70}$$

Example 1 *Let us consider the equation of elasticity on a domain $\Omega = \{(x,y) : -2 \le x, y \le 2\}$ with a crack along the negative x-axis. Assume that Young's modulus $E = 1000$, and the poisson's ratio $\nu = 0.3$. We also assume that the following true stresses are imposed along all boundaries of the given domain.*

$$\begin{aligned}
\sigma_x &= \frac{1}{4\sqrt{r}}(3\cos\frac{\theta}{2} + \cos\frac{5\theta}{2}),\\
\sigma_y &= \frac{1}{4\sqrt{r}}(5\cos\frac{\theta}{2} - \cos\frac{5\theta}{2}),\\
\tau_{xy} &= \frac{1}{4\sqrt{r}}(\sin\frac{5\theta}{2} - \sin\frac{\theta}{2}).
\end{aligned}$$

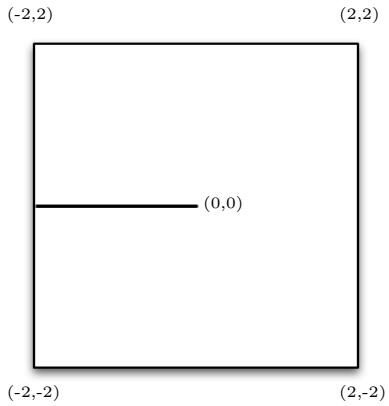

Furthermore, in order to prevent rigid body motion, the following constraints are imposed:

- *The displacement vector* $\{u\}$ *is fixed at the crack tip* $(0, 0)$.
- *The y-component of the displacement vector,* $u^y(x, y)$*, is fixed at* $(2, 2)$.

Let $\mathcal{G}$ be the following singular functions :

$$\mathcal{G} = \{\sqrt{r}cos(\frac{\theta}{2}), \sqrt{r}sin(\frac{\theta}{2}), \sqrt{r}cos(\frac{5\theta}{2}), \sqrt{r}sin(\frac{5\theta}{2})\}.$$

We pick singular functions g_i for basis enrichment from the set $\mathcal{G}$.

It is important to understand that we have the freedom to choose the set $\mathcal{G}$. For any choice for $\mathcal{G}$, one can obtain a solution that is as good as that of p-FEM that is comparable to p-version of FEM because members of $\mathcal{G}$ are additional basis functions added to the existing FEM basis.

In the extreme case, when $\mathcal{G} = \varnothing$, we get the RPP approximation which is comparable to the conventional p-FEM. Let us assume that $g \in \mathcal{G}$ was not a good choice for the given problem. That is, it does not represent the crack singularity. Then, the coefficients d_{Ji}, d_{J+1i} in (69) and (70) comes out close to zero in the finite element approximation which indicates that the corresponding enriched functions g_i, g_{i+1} were a poor choice. Hence, a prior knowledge to the solution behavior or a numerical experiment could provide an optimal or nearly optimal choice for $\mathcal{G}$.

Adding or removing one or more singular function for enrichment into $\mathcal{G}$ does not alter the background mesh that was needed to create the partition of unity. If the set $\mathcal{G}$ does generate almost exactly the stress functions $\sigma_x, \sigma_y, \tau_{xy}$ then from the coefficients d_j and d_{j+1}, one can immediately obtain the stress intensity factor (SIF) without extra cost for sophisticated post-processing.

Remark *Let us assume the set $\mathcal{G}$ can only generate the stress functions close but not exactly, then it may be possible to obtain reasonable approximation for the displacement vectors. However, the stress intensity factor does require post processing.*

In order to show the effectiveness of the proposed method, Figures 15 and 16 compare the true stress, the computed stress obtained by GFEM with enrichment, and the computed stress by the RPPM which is comparable to the standard p-version finite element methods on $[0.001, 0.01] \times [-\pi, \pi]$. In Figure 15, comparisons are for the stress σ_y, whereas Figure 16 compares the shear stress τ_{xy}.

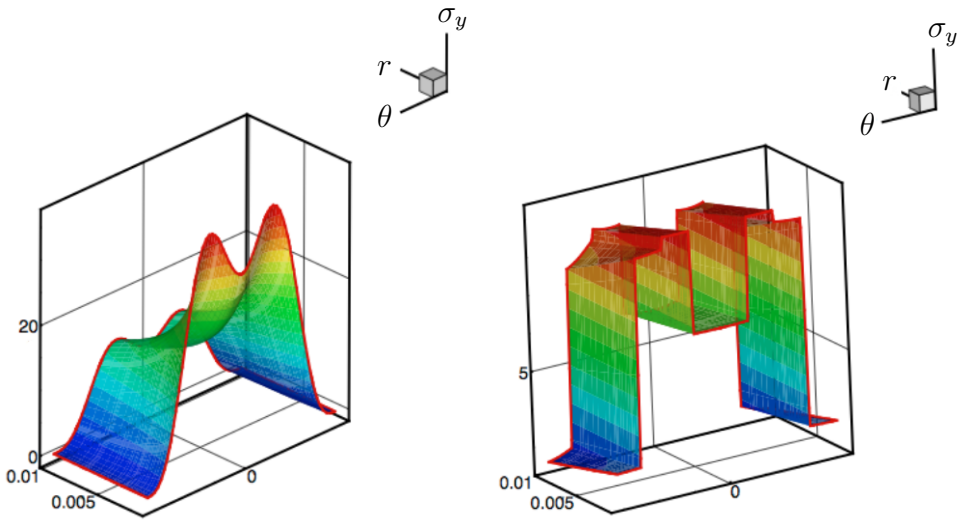

GFEM with enrichment RPPM with order 4 RPP Functions

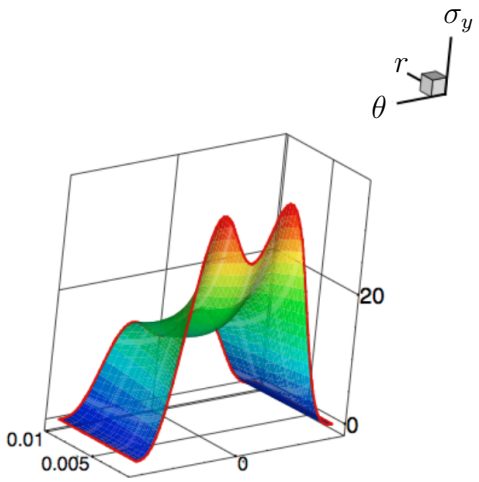

True

FIGURE 15: Stress σ_y comparison.

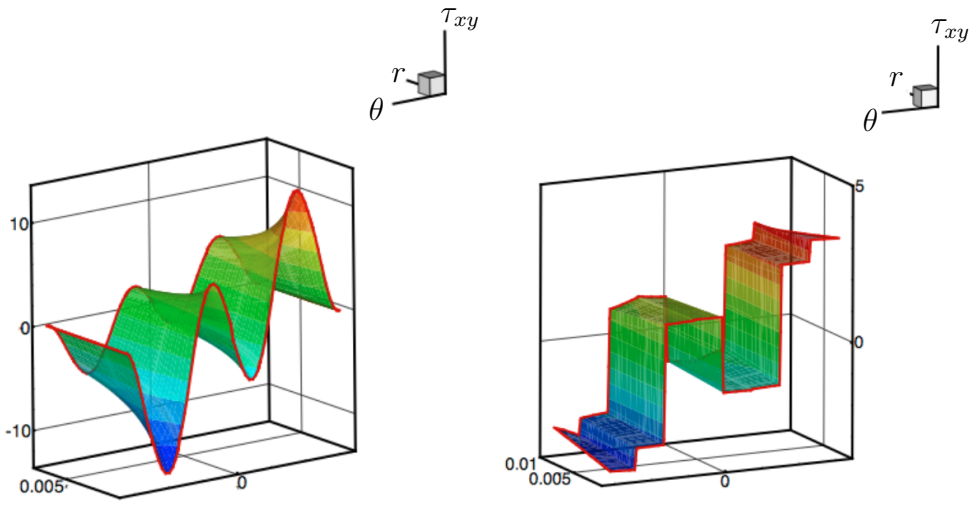

GFEM with enrichment RPPM order 4

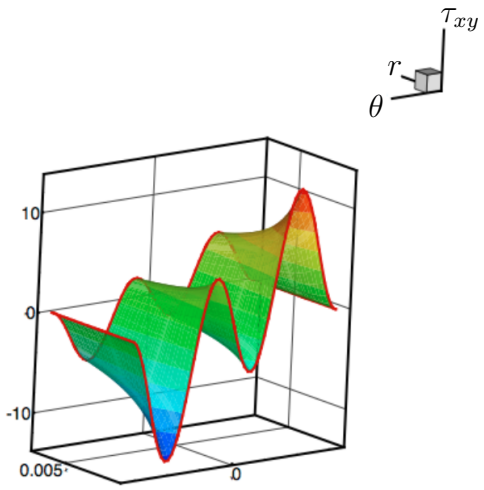

True

FIGURE 16: Stress τ_{xy} comparison.

From Figures 15 and 16, one can easily see the effectiveness of the proposed method in handling crack singularities. In other words, there is virtually no difference between the true stress and the computed stress obtained by using GFEM with enrichment. However, there is a significant difference between the computed stress and true stress by the polynomial approximation. Note the discrepancy between GFEM with enrichment and without enrichment is get larger as $r \to 0$.

Example 2 *Let us consider the equations of elasticity on a domain shown below, which is isotropic with material constants:* $E = 1000$ *and* $\nu = 0.3$. *The boundary conditions are given as follows:*

- $u_n = 0$, $u_t = 0$ *along* $\Gamma_1 \cup \Gamma_2$,
- $T_n = 10$, $T_t = 2$ *along* Γ_5,
- $T_n = 0$, $T_t = 0$ *along* $\partial\Omega \cap (\Gamma_1 \cup \Gamma_2 \cup \Gamma_5)^c$.

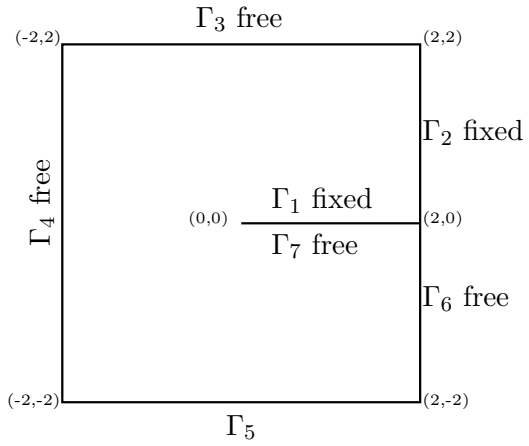

Note that this problem has a weak singularity at $(2, 2)$ and a strong singularity at the crack tip. For the conventional finite element method, two meshes, Mesh I and Mesh II, (Figure 17) are used. Mesh II is obtained from Mesh I by adding graded layers of radii $0.5, 0.5\sigma, 0.5\sigma^2, 0.5\sigma^3$ centered at crack tip and and layers of radii $0.5, 0.5\sigma, 0.5\sigma^2$ centered at top right corner, $(2, 2)$, where $\sigma = 0.15$. Mesh I and Mesh II have 22 and 48 elements, respectively.

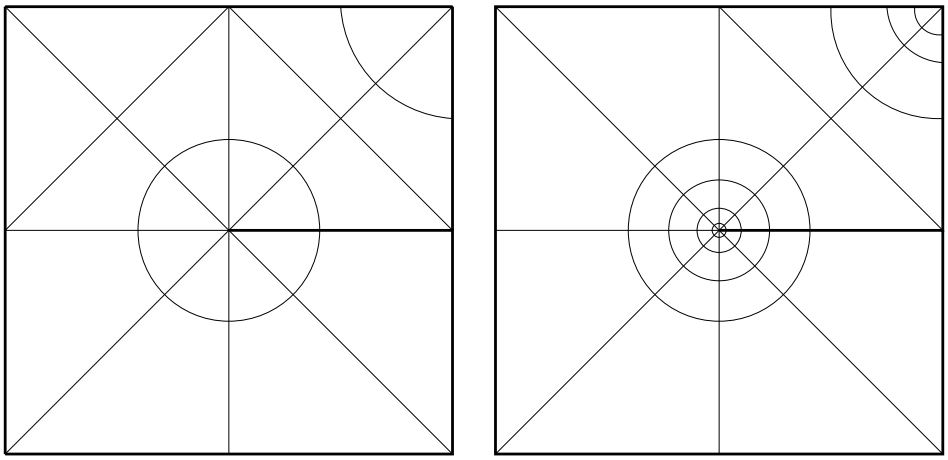

Mesh I (22 elements) Mesh II (48 elements)

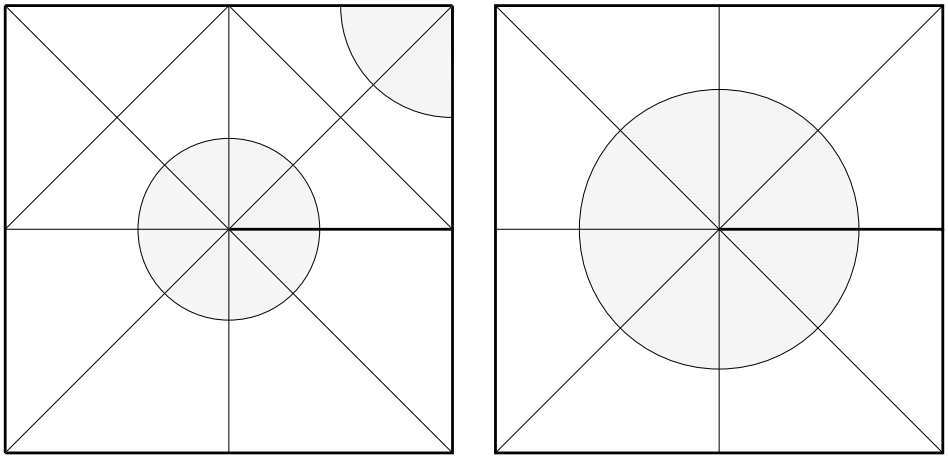

MAM with Mesh I GFEM with Enrichment

FIGURE 17: Meshes for FEM and background mesh for GFEM.

TABLE 5: Total Strain Energy Comparison.

p	***p*-FEM with Mesh I**	***p*-FEM with Mesh II**	***p*-FEM with MAM**	**GFEM with enrichment**
2	1.60551078343838	2.01871772810441	1.70213202981048	2.01441397717771
4	1.81518650351132	2.08274831820450	2.11004639654621	2.11266479436991
6	1.89915218378087	2.09344129702200	2.11356074177201	2.11380305100008
8	1.94532926077425	2.09816367972923	2.11378584006680	-

In Table 5, p-FEM with MAM (Method of Auxiliary Mapping) on Mesh I is used. For Mesh I and Mesh II, the standard p-FEM is used, without any special treatment. For the p-FEM with MAM, special mappings are used on shaded regions. The shaded region on GFEM with Enrichment is where the singular functions are used. The true energy $\mathcal{U}_{\text{exact}} = 2.113815563245032$ is obtained by the extrapolation approach given in Chapter 4 of Szabo and Babuska (1991).

For this example, only one singular enrichment function is used for enrichment, $r^{\frac{1}{3}} \sin \frac{1}{2}\theta$. The eigenvalue $\lambda = \frac{1}{3}$ is chosen because of the Dirichlet BC on Γ_1 and the Neumann BC on Γ_7. The degrees of freedom are compared in Table 6.

TABLE 6: DOF Comparison.

p	**p-FEM with Mesh I & MAM , DOF**	**p-FEM with Mesh II, DOF**	**GFEM with enrichment DOF**
2	120	280	128
4	376	792	328
6	808	1688	624
8	1416	2968	-

TABLE 7: Error Comparison in Energy Norm(%).

p	**p-FEM with Mesh I**	**p-FEM with Mesh II**	**p-FEM with MAM**	**GFEM with enrichment**
2	49.04	21.21	15.81	6.67
4	37.59	12.12	4.22	2.33
6	31.87	9.82	1.10	0.24
8	28.23	8.61	0.38	-

As shown in Table 6 and Table 7, the proposed method is not only robust, but it is highly efficient at handling elasticity problems on a cracked domain. By having the right enrichment function, the approximate solution of the GFEM with enrichment converges much faster than MAM with fewer degrees of freedom.

3.4 Meshless methods for stress intensity factors

Fracture mechanics is a mechanical framework for the behavior of cracked elastic medium under a load. Depending on what type of loading is applied to the elastic medium, the crack propagation direction may vary. Often the propagation of cracks result in total structural failure.

A principal interest in fracture mechanics is the stress intensity factor K which characterizes the stress at the crack tip in an elastic medium. There are two modes of the crack extension (Figures 18−19). Two basic modes are determined by the load that is applied to the elastic body.

- Mode I is called *the opening mode* and is due to the symmetric extension of cracked surfaces perpendicular to the plane that has crack on it. There is a displacement jump in the perpendicular direction of the cracked plane. This Mode I crack is related to K_I.

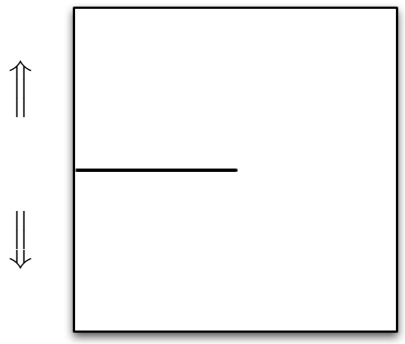

FIGURE 18: Mode I (Opening mode).

- Mode II is called *the sliding mode* and is associated with skew-symmetric loading on a cracked surface. A displacement jump arises in the parallel direction of the crack.

Since Mode I type crack extension is the most common in practice, it is regarded as

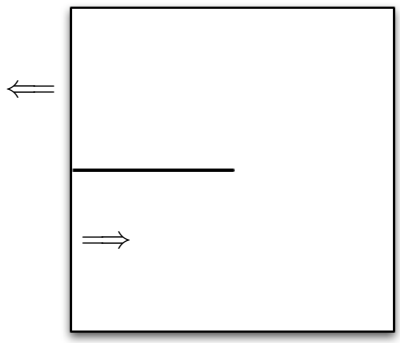

FIGURE 19: Mode II (Sliding mode).

the most important factor. In general, the stress distributions at the crack-tip are a linear combination of both modes.

If one assumes isotropic linear elastic behavior and simple geometry for the crack, it is possible to obtain closed form expression for stresses. The Westergaard's method is one such example. It is a well known fact that the stress field in a linear elastic cracked medium in the vicinity of the crack tip has the following form :

$$\sigma_{ij} = \frac{K}{\sqrt{2\pi r}} f_{ij}(\theta) + \cdots \tag{71}$$

where σ_{ij} are components of the stress tensor, f_{ij} is a dimensionless function of θ, and (r, θ) is the polar coordinates that has the origin at the crack tip.

The stress distribution in the vicinity of a crack tip can be completely determined by the stress intensity factor K when the Mode is specified. Hence, it is clear that when K is given, all components of stress, strain, and displacements will be resolved. It is known that the crack grows when K exceeds some critical value, K_c. As a matter of fact, this critical value K_c does not depend on the geometry of the crack, but it is a material property.

To determine whether a crack will grow or not is determined by K_c and K. In practice, K_c is obtained by an experiment on cracked specimens of the elastic material. Whereas the stress intensity factor K can be obtained by applying numerical methods

or analytically.

The conventional finite element method is a powerful tool; however it is not efficient for crack problems because of its slow convergence. The inefficiency is due to the existence of the singular stress field in the vicinity of a crack-tip. Although many approaches have been introduced, no efficient and universal approach has emerged to estimate accurate stress intensity factor. In this dissertation, a different attempt has been made to obtain the stress intensity factor and is compared to conventional approaches.

Although applying the conventional finite element method is straightforward, the obvious disadvantage is that it requires an extremely fine finite element mesh around the crack tip in order to capture the behavior of the singular stress field. In an effort to provide accurate and economical approximations, various attempts have been made over the years to deal with a singularity in elasticity problems. There are three ways the problem is approached: mesh refinement, incorporating special singular elements, and using nonlocal special singular functions.

Of course, adding special singular functions that mimic the behavior of the singularities into the approximation space will greatly enhance the solution, but the implementation would be extremely difficult. In addition, one must get the eigenvalues corresponding to the singular points to choose the right singular functions. Therefore, the most popular choices would be mesh refinement or adaptive finite element methods; however its success relies on a proper choice of mesh, and it also requires lengthy computing time.

On the other hand, the p-FEM with MAM approach is capable to yield very accurate solutions successfully (Oh and Babuska, 1995). It was shown that this approach gives superior results to other methods with almost no extra cost. Moreover, this method gives a reasonable solution for those elasticity problems even when the h-p version of the finite element method failed. Despite the fact that the MAM method

has the ability to resolve an accurate stress fields in the vicinity of the crack-tip and accurate calculation for the stress intensity factor, it has the following shortcoming: First, to accurately estimate the stress intensity factor it requires sophisticated post processing. Second, capturing an oscillating singularity such as in bi-material cracks would be difficult.

Using the GFEM with enrichment, the exact singular behavior of the stress field around the crack tip can be embedded in the basis functions whether it is an oscillating singularity or a monotone singularity. Hence, the proposed meshless method yields highly accurate solutions like p-FEM with MAM, but it is more robust and has the extra ability to capture oscillating singularities.

In summary, the advantage of using the meshless method with enrichment for elasticity problems on a cracked elastic medium is the ability to use the exact singular functions as local shape functions. Also it is possible to obtain the stress intensity factor directly as apposed to the conventional methods.

As mentioned in the previous chapter, the present method has the flexibility to choose local approximation functions on each patch differently. In the vicinity of the crack-tip region, enrichment with singular functions can be easily adopted. To that end, we make asymptotic expansions of the displacement vector in the vicinity of crack tip and use influential terms of this expansion as enrichment functions. Choosing the correct enriched function, one can directly obtain the stress intensity factor (SIF) without any post-processing such as is necessary in conventional finite element methods.

For simplicity, let us assume that there is no body force. The displacement vector can be defined as follows(Szabo and Babuska, 1991).

$$\begin{cases} u^s(r,\theta) &= u_0^s + \sum_{k=1}^{\infty} A_k^{(1)} u_k^{s(1)}(r,\theta) + \sum_{k=1}^{\infty} A_k^{(2)} u_k^{s(2)}(r,\theta), \\ u^t(r,\theta) &= u_0^t + \sum_{k=1}^{\infty} A_k^{(1)} u_k^{t(1)}(r,\theta) + \sum_{k=1}^{\infty} A_k^{(2)} u_k^{t(2)}(r,\theta), \end{cases} \tag{72}$$

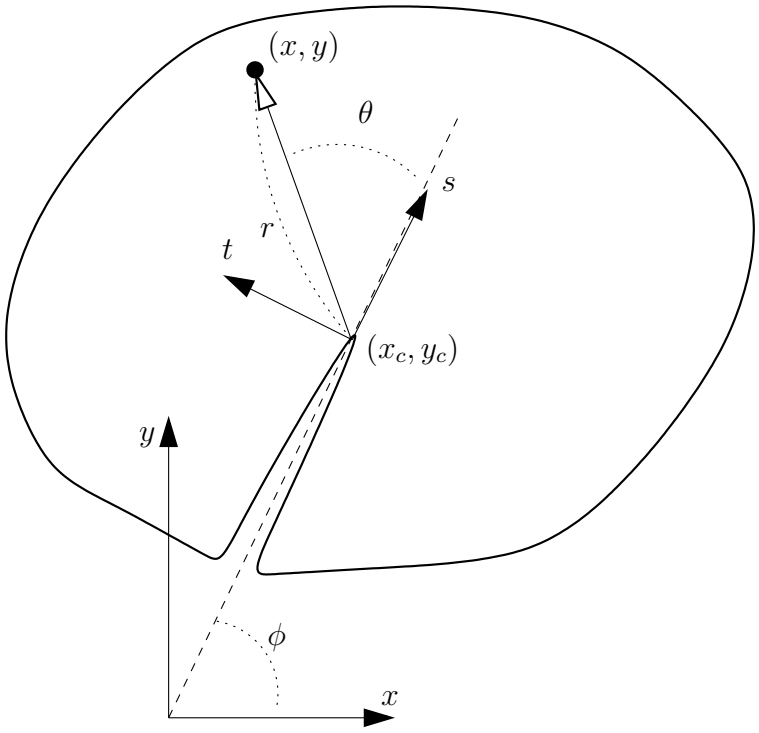

FIGURE 20: Coordinate systems in the vicinity of crack-tip.

where the superscripts (1) and (2) denote symmetric and anti-symmetric parts, respectively. The $u_k^{s(1)}, u_k^{s(2)}, u_k^{t(1)}, u_k^{t(2)}$ are defined as follows.

$$u_k^{s(1)} = \frac{1}{2G} r^{\lambda_k} [(\kappa - Q_k^{(1)}(\lambda_k + 1)) \cos \lambda_k \theta - \lambda_k \cos(\lambda_k - 2)\theta] \tag{73}$$

$$u_k^{t(1)} = \frac{1}{2G} r^{\lambda_k} [(\kappa + Q_k^{(1)}(\lambda_k + 1)) \sin \lambda_k \theta + \lambda_k \sin(\lambda_k - 2)\theta] \tag{74}$$

$$u_k^{s(2)} = \frac{1}{2G} r^{\lambda_k} [(\kappa - Q_k^{(2)}(\lambda_k + 1)) \sin \lambda_k \theta - \lambda_k \sin(\lambda_k - 2)\theta] \tag{75}$$

$$u_k^{t(2)} = \frac{-1}{2G} r^{\lambda_k} [(\kappa + Q_k^{(2)}(\lambda_k + 1)) \cos \lambda_k \theta + \lambda_k \cos(\lambda_k - 2)\theta] \quad , \tag{76}$$

where $Q_k^{(1)}$, $Q_k^{(2)}$, and eigenvalues λ_k are the following.

$$\lambda_1 = \frac{1}{2} \text{ and } \lambda_k = \frac{k+1}{2} \text{ for } k \geq 2 \quad , \tag{77}$$

$$Q_k^{(1)} = \begin{cases} -1 & \text{for} \quad k = 2n - 1 (n \geq 2) \\ \dfrac{1 - \lambda_k}{1 + \lambda_k} & \text{for} \quad k = 1 \text{ and } k = 2n (n \geq 1) \end{cases} \quad , \tag{78}$$

$$Q_k^{(2)} = \begin{cases} \dfrac{1-\lambda_k}{1+\lambda_k} & \text{for} \quad k = 2n-1 (n \geq 2) \\ -1 & \text{for} \quad k = 1 \text{ and } k = 2n (n \geq 1) \end{cases} . \tag{79}$$

G is the shear modulus defined by Young's modulus E and Poisson's ratio ν as follows:

$$G = \frac{E}{2(1+\nu)}$$

The constant κ shown in (73)-(76) is determined by Poisson's ratio ν as the following. Depending on whether plane strain or plane stress is considered. For plane strain, we have

$$\kappa = 3 - 4\nu$$

and for the plane stress,

$$\kappa = \frac{3-\nu}{1+\nu}.$$

The coefficients $A_1^{(1)}, A_1^{(2)}$ are called the *generalized stress intensity factors* and are related to the Mode I and Mode II stress intensity factors of linear elastic fracture mechanics, usually denoted by symmetric mode K_I and anti-symmetric mode K_{II}. The definition of K_I and K_{II} follows:

$$A_1^{(1)} = \frac{K_I}{\sqrt{2\pi}}, \qquad A_1^{(2)} = \frac{K_{II}}{\sqrt{2\pi}}. \tag{80}$$

Note (73)-(76) is expressed in terms of polar coordinates but these could be easily interchanged to rectangular coordinate using following transformations.

$$\begin{cases} r &= \sqrt{s^2+t^2} \\ \theta &= \arctan\left(\frac{t}{s}\right) \end{cases} ; \qquad \begin{cases} s &= (x-x_c)\cos\phi &+ &(y-y_c)\sin\phi \\ t &= -(x-x_c)\sin\phi &+ &(y-y_c)\cos\phi \end{cases} . \tag{81}$$

Similarly, the displacements near the crack-tip region can be transformed in the following way:

$$\begin{cases} u_k^{x(l)} &= u_k^{s(l)}\cos\phi &- &u_k^{t(l)}\sin\phi \\ u_k^{y(l)} &= u_k^{s(l)}\sin\phi &+ &u_k^{t(l)}\cos\phi \end{cases} \tag{82}$$

where $l = 1, 2$ and $k = 1, \cdots, \infty$.

Therefore, using (82), the displacement vector (72) transforms in terms of the x-y coordinates as follows:

$$\begin{cases} u^x &= u_0^x + \sum_{k=1}^{\infty}[A_k^{(1)} u_k^{x(1)} + A_k^{(2)} u_k^{x(2)}] \\ u^y &= u_0^y + \sum_{k=1}^{\infty}[A_k^{(1)} u_k^{y(1)} + A_k^{(2)} u_k^{y(2)}] \end{cases} \tag{83}$$

Truncating (83) to a finite sum will reveal the enrichment functions. More specifically, for the x-displacement we choose $\{u_k^{x(1)}, u_k^{x(2)}, k = 1, \cdots, N\}$ as enrichment functions and for the y-displacement, one may choose $\{u_k^{y(1)}, u_k^{y(2)}, k = 1, \cdots, N\}$ as enrichment functions. Note that the coefficients of $u_k^{x(1)}$ and $u_k^{y(1)}$ are the generalized stress intensity factors. Hence, if the GFEM approximation space explicitly contains the functions $u_k^{x(l)}$ and $u_k^{y(l)}$, then the stress intensity factor(SIF) can be obtained by reading the amplitude of the enriched functions. If the test space does not contain $u_k^{x(l)}$ and $u_k^{y(l)}$, then the stress intensity factor could be estimated as follows:

Let G be the *Strain Energy Release Rate* and U be the elastic strain energy. Then in two-dimensional case where the crack extends along its own direction in a self-similar manner, the central difference approximation (CDA) could be used for the energy release rate as follows:

$$G \approx \frac{U(a + \Delta) - U(a - \Delta)}{2\Delta}, \tag{84}$$

for a smaller number Δ. However, this approach has two drawbacks. First, in (84), one is forced to divide a huge number with a small number which results in inaccuracy. Second, to accomplish this procedure one needs to run the FE code twice.

On the other hand, there is another well known method, the virtual crack closure technique (VCCT). The following two integrals give the energy release rates of the

opening mode (Mode I) and the sliding mode (Mode II), respectively:

$$G_I \approx \frac{1}{2\Delta}\int_0^{\Delta} \sigma_y(r,0)[u_y(\Delta - r,\pi) - u_y(\Delta - r,-\pi)]dr, \tag{85}$$

$$G_{II} \approx \frac{1}{2\Delta}\int_0^{\Delta} \tau_{xy}(r,0)[u_x(\Delta - r,\pi) - u_x(\Delta - r,-\pi)]dr. \tag{86}$$

Although the sum of G_I and G_{II}, total energy release rate G, does converge as $\Delta \to 0$, each of the integrals usually do not converge for the interfacial cracks between dissimilar materials due to the oscillatory nature of the stress and displacement fields in the vicinity of the crack tip. In this dissertation, we deal with cracks in homogeneous materials. So both G_I and G_{II} do converge. Again, it is important to note that this post processing is not necessary when we utilize the correct enriched functions.

Remark *To get the accurate stress intensity factors, it is important to choose the correct pairs of enrichment functions for the x and y directions. In other words, unlike the conventional FEM basis functions constructed in section 3.1, the basis functions for the x-displacement are different from the basis functions for the y-displacement. However, to obtain the stress intensity factor in the proposed way, one must be extremely careful in selecting local approximation functions near the crack-tip. This will be discussed in more detail in the following example.*

Example 3 *Single edge-notched specimen (SENS) : Let us consider a single edge-notched plate* $[-a, b-a] \times [-k, k]$ *under uniform tension S as Figure 21. It is known that the mode I stress intensity factor for single edge-notched plate is the following (Gdoutos, 1993),*

$$K_I = S\sqrt{\pi a}\{1.12 - 0.23(\frac{a}{b}) + 10.55(\frac{a}{b})^2 - 21.72(\frac{a}{b})^3 + 30.39(\frac{a}{b})^4\}, \tag{87}$$

whenever $0 < \dfrac{a}{b} < 0.6$.

In this example, $a = 0.55$, $b = 1.0$, $k = 2.0$, $E = 10^6$, and uniform traction $S = 100$ is used. Using (87), we have $K_I = 440.6271928$ and $G_I = (1-\nu^2)\frac{K_I^2}{E} = 0.176678$. The

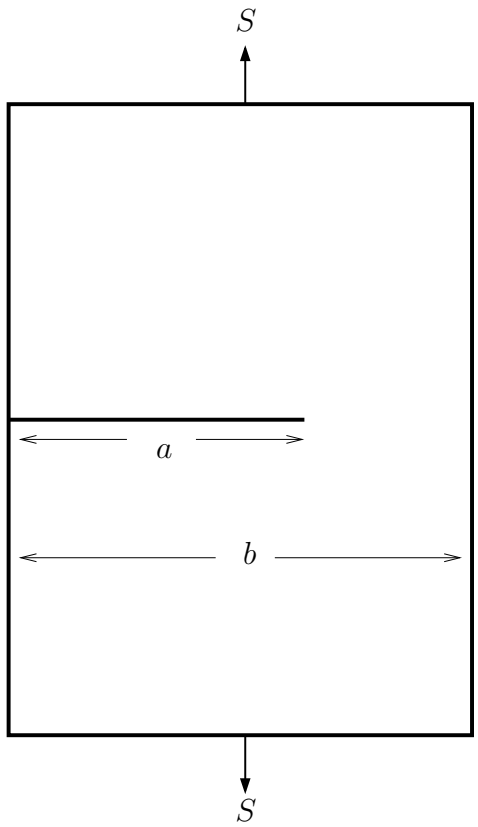

FIGURE 21: Single edge-notched specimen (SENS).

results are presented in Table 8, from which we can verify the superiority of proposed method. All entries have been calculated using (84) with $\Delta = 0.5 \times 10^{-8}$.

TABLE 8: Plain strain computation for single edge-notched plate.

p	G_{p-FEM}	G_{MAM}	G_{ENRICH}
2	0.1270484	0.1501532	0.1748723
4	0.1378598	0.1721155	0.1754336
6	0.1473620	0.1754222	0.1763207
8	0.1535316	0.1755709	-

For the conventional finite element method, eight triangular elements are used around the crack tip and for the rest the region, 28 quadrilateral elements are used. For MAM solutions, we choose eight inner triangular regions as the mapping zone. For the GFEM with enrichment, the same background mesh is used as that of Example 2. The following enrichment functions are used to enrich the existing basis functions

around the crack tip singularity.

$$\mathcal{G} = \{\sqrt{r}cos(\frac{\theta}{2}), \sqrt{r}sin(\frac{\theta}{2}), \sqrt{r}cos(\frac{5\theta}{2}), \sqrt{r}sin(\frac{5\theta}{2})\}.$$

Although the previously used enrichment functions $\mathcal{G}$ are good enough to capture the singular behavior of the stress field in the vicinity of the crack tip. To obtain the stress intensity factor, we need to use (84) or (85) and (86) in the post processing. These methods will certainly give correct stress intensity factors; however if we choose an appropriate enrichment space, we can avoid this post processing to estimate the stress intensity factor. Details follow as shown in the following example.

Example 4 *Consider the elasticity problem on the cracked domain discussed in Example 1. We directly calculate the stress intensity factor of the problem by calculating the amplitudes of the leading coefficients. To see the effectiveness of the proposed stress intensity factor calculation, let us revisit Example 1. Note the imposed stresses are Mode I with* $K_I = 1$ *(See Exercise 10.4, (Szabo and Babuska, 1991)).*

In Figure 20, the crack is aligned parallel to the x-axis. i.e. $\phi \equiv 0$. Hence $s \equiv x$ and $t \equiv y$. Having this fact we can rewrite (72)-(75) in the following way.

$$\begin{cases} u^x(r,\theta) &= u_0^x + \sum_{k=1}^{\infty} A_k^{(1)} u_k^{x(1)}(r,\theta) + \sum_{k=1}^{\infty} A_k^{(2)} u_k^{x(2)}(r,\theta) \\ u^y(r,\theta) &= u_0^y + \sum_{k=1}^{\infty} A_k^{(1)} u_k^{y(1)}(r,\theta) + \sum_{k=1}^{\infty} A_k^{(2)} u_k^{y(2)}(r,\theta), \end{cases} \tag{88}$$

where the superscripts (1) and (2) denote the symmetric and anti-symmetric parts, respectively. The $u_k^{x(1)}, u_k^{x(2)}, u_k^{y(1)}, u_k^{y(2)}$ are defined as follows.

$$u_k^{x(1)} = \frac{1}{2G} r^{\lambda_k} [(\kappa - Q_k^{(1)}(\lambda_k + 1)) \cos \lambda_k \theta - \lambda_k \cos(\lambda_k - 2)\theta] \tag{89}$$

$$u_k^{y(1)} = \frac{1}{2G} r^{\lambda_k} [(\kappa + Q_k^{(1)}(\lambda_k + 1)) \sin \lambda_k \theta + \lambda_k \sin(\lambda_k - 2)\theta] \tag{90}$$

$$u_k^{x(2)} = \frac{1}{2G} r^{\lambda_k} [(\kappa - Q_k^{(2)}(\lambda_k + 1)) \sin \lambda_k \theta - \lambda_k \sin(\lambda_k - 2)\theta] \tag{91}$$

$$u_k^{y(2)} = \frac{-1}{2G} r^{\lambda_k} [(\kappa + Q_k^{(2)}(\lambda_k + 1)) \cos \lambda_k \theta + \lambda_k \cos(\lambda_k - 2)\theta] \tag{92}$$

By plugging (80) into (88), we have the following. For brevity, (r, θ) is suppressed.

$$\begin{cases} u^x(r,\theta) &= u_0^x + \dfrac{K_I}{\sqrt{2\pi}} u_1^{x(1)} + \dfrac{K_{II}}{\sqrt{2\pi}} u_1^{x(2)} + \displaystyle\sum_{k=2}^{\infty} A_k^{(1)} u_k^{x(1)} + \sum_{k=2}^{\infty} A_k^{(2)} u_k^{x(2)} \\ u^y(r,\theta) &= u_0^y + \dfrac{K_I}{\sqrt{2\pi}} u_1^{y(1)} + \dfrac{K_{II}}{\sqrt{2\pi}} u_1^{y(2)} + \displaystyle\sum_{k=2}^{\infty} A_k^{(1)} u_k^{y(1)} + \sum_{k=2}^{\infty} A_k^{(2)} u_k^{y(2)} \end{cases} \tag{93}$$

In this specific example only Mode I tractions are applied. So the displacements do not have the terms that have superscript (2) in (93).

$$\begin{cases} u^x(r,\theta) &= u_0^x + \dfrac{K_I}{\sqrt{2\pi}} u_1^{x(1)} + \displaystyle\sum_{k=2}^{\infty} A_k^{(1)} u_k^{x(1)} \\ u^y(r,\theta) &= u_0^y + \dfrac{K_I}{\sqrt{2\pi}} u_1^{y(1)} + \displaystyle\sum_{k=2}^{\infty} A_k^{(1)} u_k^{y(1)} \end{cases} \tag{94}$$

Also by neglecting the rigid body motion and $K_I = 1$, (94) becomes,

$$\begin{cases} u^x(r,\theta) &= \dfrac{1}{\sqrt{2\pi}} u_1^{x(1)} + \underbrace{\displaystyle\sum_{k=2}^{\infty} A_k^{(1)} u_k^{x(1)}}_{(a)} \\ u^y(r,\theta) &= \dfrac{1}{\sqrt{2\pi}} u_1^{y(1)} + \underbrace{\displaystyle\sum_{k=2}^{\infty} A_k^{(1)} u_k^{y(1)}}_{(b)} . \end{cases} \tag{95}$$

Choosing appropriate enriched functions becomes obvious if one carefully examines (95). If the approximation space contains,

$$\frac{1}{\sqrt{2\pi}} u_1^{x(1)}(r,\theta), \quad \frac{1}{\sqrt{2\pi}} u_1^{y(1)}(r,\theta)$$

then the amplitude of the finite element approximation of these functions will reveal stress intensity factor K_I. For this specific problem the amplitude should be 1. Indeed, the success of this method heavily depends on how well the RPP approximation will capture the series terms, (a) and (b), presented in (95). Therefore, for low order RPP approximation more enrichment functions are required to get the stress intensity factor correctly.

Remark *It is important to choose a different approximation spaces for x-displacement*

and y-displacement to get the stress intensity factor in the proposed way. This, however, does not increase the computational load significantly because the non-symmetric part only comes from the enriched functions. Note most of basis functions for x-displacement and y-displacement are the same except for the enriched functions.

From (77)-(79), we obtain the following.

$$\begin{aligned} \lambda_1^{(1)} &= \frac{1}{2}, \lambda_2^{(1)} = \frac{3}{2}, \lambda_3^{(1)} = 2, \lambda_4^{(1)} = \frac{5}{2}, \lambda_5^{(1)} = 3, \cdots \\ Q_1^{(1)} &= \frac{1}{3}, Q_2^{(1)} = -\frac{1}{5}, Q_3^{(1)} = -1, Q_4^{(1)} = -\frac{3}{7}, Q_5^{(1)} = -1, \cdots . \end{aligned}$$

Therefore, we choose the following ten singular functions as enrichment for the x-displacement and the y-displacement, respectively.

$$\mathcal{G}^x = \{\frac{1}{2G\sqrt{2\pi}} r^{\frac{1}{2}}((\kappa - \frac{1}{2})\cos\frac{\theta}{2} - \frac{1}{2}\cos\frac{3\theta}{2}), \frac{1}{2G\sqrt{2\pi}} r^{\frac{3}{2}}((\kappa + \frac{1}{2})\cos\frac{3\theta}{2} - \frac{3}{2}\cos\frac{\theta}{2}),$$
$$\cdots, \frac{1}{2G\sqrt{2\pi}} r^3((\kappa + 3)\cos 3\theta - 3\cos\theta)\},$$

$$\mathcal{G}^y = \{\frac{1}{2G\sqrt{2\pi}} r^{\frac{1}{2}}((\kappa + \frac{1}{2})\sin\frac{\theta}{2} - \frac{1}{2}\sin\frac{3\theta}{2}), \frac{1}{2G\sqrt{2\pi}} r^{\frac{3}{2}}((\kappa - \frac{1}{2})\sin\frac{3\theta}{2} - \frac{3}{2}\sin\frac{\theta}{2}),$$
$$\cdots, \frac{1}{2G\sqrt{2\pi}} r^3((\kappa - 3)\sin 3\theta + 3\sin\theta)\}.$$

The following table shows the stress intensity factor obtained by the proposed method without post processing. The amplitude of the $\frac{1}{\sqrt{2\pi}} u_1^{x(1)}(r,\theta)$ is listed in Table 9 with respect to various RPP orders. The exact stress intensity factor K_I for this specific example is 1. Table 9 support that the proposed method to compute the SIF is reliable.

TABLE 9: Stress Intensity Factor of Example 4.

p	**SIF** (K_I)
2	0.99543
4	1.00178
6	1.00024

REFERENCES

Atluri, A. and S. Shen. *The Meshless Method*. Tech Science Press, 2002.

Babuska, I., U. Banerjee, and J. E. Osborn. On principles for the selection of shape functions for the generalized finite element method. *Computer Methods in Applied Mechanics and Engineering*, 191(49-50):5595 – 5629, 2002. ISSN 0045-7825.

Babuska, I., U. Banerjee, and J. E. Osborn. Survey of meshless and generalized finite element methods: A unified approach. *Acta Numerica*, 12(-1):1–125, 2003.

Babuska, I., U. Banerjee, and J. Osborn. Generalized finite element methods main ideas, results and perspective. *International Journal of Computational Methods*, 1 (1):67 – 103, 2004.

Babuska, I., V. Nistor, and N. Tarfulea. Generalized finite element method for second-order elliptic operators with dirichlet boundary conditions. *Journal of Computational and Applied Mathematics*, 218(1):175 – 183, 2008. ISSN 0377-0427.

Ciarlet, P. *Basis Error Estimates for Elliptic Problems*, volume II. North Holland, 1991.

Duarte , C. A. and J. T. Oden. An h-p adaptive method using clouds. *Computer Methods in Applied Mechanics and Engineering*, 139(1-4):237 – 262, 1996. ISSN 0045-7825.

Gdoutos, E. *Fracture Mechanics: An Introduction*. Kluwer Academic Publishers, 1993.

Georgiou,G. , L. Olsen, and Y. S. Smyrlis. A singular function boundary integral method for the laplace equation. *Communications in numerical methods in engineering*, 12:127–134, 1996.

Han, W. and X. Meng. Error analysis of the reproducing kernel particle method. *Computer Methods in Applied Mechanics and Engineering*, 190(46-47):6157 – 6181, 2001. ISSN 0045-7825.

Hendry, J. A. and L. M. Delves. The global element method applied to a harmonic mixed boundary value problem. *Journal of Computational Physics*, 33(1):33 – 44, 1979. ISSN 0021-9991.

Höllig, K. *Finite Element Methods with B-Splines*. Society for Industrial and Applied Mathematics, 2003. ISBN 0898715334.

Kermode, M., A. McKerrell, and L. M. Delves. The calculation of singular coefficients. *Computer Methods in Applied Mechanics and Engineering*, 50(3):205 – 215, 1985. ISSN 0045-7825.

Lancaster, P. and K. Salkauskas. Surfaces generated by moving least squares methods. *Mathematics of Computation*, 37(155):141–158, 1981. ISSN 00255718.

Levin, D. The approximation power of moving least-squares. *Math. Comput.*, 67 (224):1517–1531, 1998. ISSN 0025-5718.

Li, S. and W. K. Liu. *Meshfree Particle Methods*. Springer, 2004. ISBN 9783540222569.

Li, S. H. Lu, W. Han, W. K. Liu, and D. C. Simkins. Reproducing kernel element method part ii: Globally conforming im/cn hierarchies. *Computer Methods in Applied Mechanics and Engineering*, 193(12-14):953 – 987, 2004. ISSN 0045-7825.

Li, Z. R. Mathon, and P. Sermer. Boundary methods for solving elliptic problems with singularities and interfaces. *Siam Journal On Numerical Analysis*, 24(3):487–498, JUN 1987.

Liu, W.K., W. Han, H. Lu, S. Li, and J. Cao. Reproducing kernel element method. part i: Theoretical formulation. *Computer Methods in Applied Mechanics and Engineering*, 193(12-14):933 – 951, 2004. ISSN 0045-7825.

Lu, T. T., H. Y. Hu, and Z. C. Li. Highly accurate solutions of motz's and the cracked beam problems. *Engineering Analysis with Boundary Elements*, 28(11): 1387 – 1403, 2004. ISSN 0955-7997.

Lucas, T.R. and H. S. Oh. The method of auxiliary mapping for the finite element solutions of elliptic problems containing singularities. *Journal of Computational Physics*, 108(2):327 – 342, 1993. ISSN 0021-9991.

Melenk, J.M., I. Babuska, E. T. Hochschule, and E. T. Hochschule. The partition of unity finite element method: Basic theory and applications, 1996.

Morley. Finite element solution of boundary-value problems with non-removable singularities. *Phil. Trans. R. Soc. Lond. A*, 275(463), 1973.

Motz, M. The treatment of singularities of partial differential equations by relaxation methods. *Q Appl Math*, 4:371–377, 1947.

Oh, H.-S. and I. Babuska. The method of auxiliary mapping for the finite element solutions of elasticity problems containing singularities. *Journal of Computational*

Physics, 121(2):193 – 212, 1995. ISSN 0021-9991. doi: DOI: 10.1016/S0021-9991(95)90017-9.

Oh, H.-S. and J. W. Jeong. Reproducing polynomial (singularity) particle methods and adaptive meshless methods for two-dimensional elliptic boundary value problems. *Computer Methods in Applied Mechanics and Engineering*, 198(9-12):933 – 946, 2009. ISSN 0045-7825. doi: DOI: 10.1016/j.cma.2008.11.005.

Oh, H.-S. and J. W. Jeong. Almost everywhere partition of uninity to deal with essential boundary conditions in meshless methods. *Computer Methods in Applied Mechanics and Engineering*, submitted, 2008.

Oh, H.-S. , J. G. Kim, and S. S. Yum. The weighted finite element method for elasticity equations on unbounded domains. *Computer Methods in Applied Mechanics and Engineering*, 152(1-2):259 – 280, 1998. ISSN 0045-7825. doi: DOI: 10.1016/S0045-7825(97)00193-X. Containing papers presented at the Symposium on Advances in Computational Mechanics.

Oh, H.-S. , H. Kim, and S.-J. Lee. The numerical methods for oscillating singularities in elliptic boundary value problems. *J. Comput. Phys.*, 170(2):742–763, 2001. ISSN 0021-9991. doi: http://dx.doi.org/10.1006/jcph.2001.6759.

Oh, H.-S. , J. G. Kim, and J. Jeong. The closed form reproducing polynomial particle shape functions for meshfree particle methods. *Computer Methods in Applied Mechanics and Engineering*, 196(35-36):3435 – 3461, 2007a. ISSN 0045-7825.

Oh, H.-S. , J. G. Kim, and J. W. Jeong. The closed form reproducing polynomial particle shape functions for meshfree particle methods. *Computational Mechanics*, 40(12):3435–3461, 2007b.

Oh, H.-S. , J. G. Kim, and W.-T. Hong. The piecewise polynomial partition of unity functions for the generalized finite element methods. *Computer Methods in Applied Mechanics and Engineering*, 197(45-48):3702 – 3711, 2008. ISSN 0045-7825.

Oh, H.-S. , J. W. Jeong, and W.-T. Hong. The generalized product partition of unity for the meshless methods, http://www.math.uncc.edu/∼hso/publications.html. *Journal of Computational Physics*, submitted, 2009.

Olson, L. G. , G. C. Georgiou, and W. W. Schultz. An efficient finite element method for treating singularities in laplace's equation. *Journal of Computational Physics*, 96(2):391 – 410, 1991. ISSN 0021-9991.

Rosse, J. B. and N. Papamichael. A power series solution of a harmonic mixed boundary value problem. *Technical summary report*, 1975.

Strouboulis, T., L. Zhang, and I. Babuska. Generalized finite element method using mesh-based handbooks: application to problems in domains with many voids. *Computer Methods in Applied Mechanics and Engineering*, 192(28-30):3109 – 3161, 2003. ISSN 0045-7825.

Szabo, B. and I. Babuska. *Finite Element Analysis*. John Wiley, 1991.

Wait, R. and A. R. Mitchell. Corner singularities in elliptic problems by finite element methods. *Journal of Computational Physics*, 8(1):45 – 52, 1971. ISSN 0021-9991.

Whiteman, J.R. Finite-difference techniques for a harmonic mixed boundary problem having a reentrant boundary. *Proc. R. Soc. Lond. A*, 1553(323), 1971.

Wigley, N. M. An efficient method for subtracting off singularities at corners for laplace's equation. *Journal of Computational Physics*, 78(2):369 – 377, 1988. ISSN 0021-9991.